J. Fluid Mech. (2024), *vol*. 997, A33, doi:10.1017/jfm.2024.601

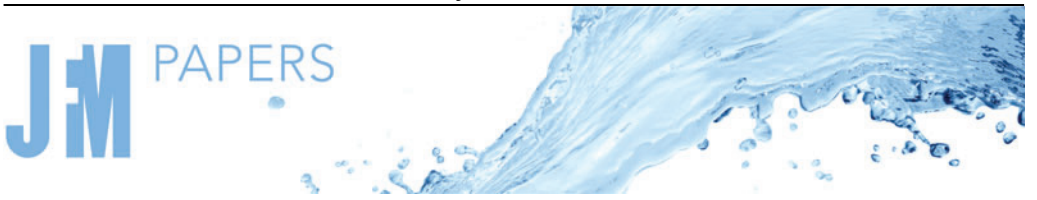

Field investigation of 3-D snow settling dynamics under weak atmospheric turbulence

Jiaqi Li[1,2], **Michele Guala**[1,3] **and Jiarong Hong**[1,2,†]

[1]Saint Anthony Falls Laboratory, University of Minnesota, Minneapolis, MN 55414, USA

[2]Department of Mechanical Engineering, University of Minnesota, Minneapolis, MN 55455, USA

[3]Department of Civil, Environmental, and Geo- Engineering, University of Minnesota, Minneapolis, MN 55455, USA

(Received 14 March 2024; revised 1 August 2024; accepted 4 August 2024)

Research on the settling dynamics of snow particles, considering their complex morphologies and real atmospheric conditions, remains scarce despite extensive simulations and laboratory studies. Our study bridges this gap through a comprehensive field investigation into the three-dimensional (3-D) snow settling dynamics under weak atmospheric turbulence, enabled by a 3-D particle tracking velocimetry (PTV) system to record over a million trajectories, coupled with a snow particle analyser for simultaneous aerodynamic property characterization of four distinct snow types (aggregates, graupels, dendrites, needles). Our findings indicate that while the terminal velocity predicted by the aerodynamic model aligns well with the PTV-measured settling velocity for graupels, significant discrepancies arise for non-spherical particles, particularly dendrites, which exhibit higher drag coefficients than predicted. Qualitative observations of the 3-D settling trajectories highlight pronounced meandering in aggregates and dendrites, in contrast to the subtler meandering observed in needles and graupels, attributable to their smaller frontal areas. This meandering in aggregates and dendrites occurs at lower frequencies compared with that of graupels. Further quantification of trajectory acceleration and curvature suggests that the meandering frequencies in aggregates and dendrites are smaller than that of morphology-induced vortex shedding of disks, likely due to their rotational inertia, and those of graupels align with the small-scale atmospheric turbulence. Moreover, our analysis of vertical acceleration along trajectories elucidates that the orientation changes in dendrites and aggregates enhance their settling velocity. Such insights into settling dynamics refine models of snow settling velocity under weak

† Email address for correspondence: jhong@umn.edu

atmospheric turbulence, with broader implications for more accurately predicting ground snow accumulation.

Key words: atmospheric flows, particle/fluid flow

1. Introduction

Understanding the intricacies of snow settling dynamics is critical for accurately modelling snow accumulation, which has various scientific and socio-economic implications. These include issuing natural hazard warnings such as avalanches (Steinkogler, Sovilla & Lehning 2014) and snow-melt floods (Marks *et al.* 1998), understanding snow hydrology and its influence on local climates (Clark *et al.* 2011), and optimizing traffic management during snow events (Ogura *et al.* 2002). A crucial determinant in the rate of snow accumulation is the settling velocity of snow particles, which can vary significantly, ranging from $0.5\,\mathrm{m\,s^{-1}}$ to speeds exceeding $3\,\mathrm{m\,s^{-1}}$ (Garrett & Yuter 2014; Nemes *et al.* 2017; Li *et al.* 2021*a*). This variability greatly influences the drift distance of snowflakes as they descend from clouds to the ground. Presently, weather forecast models often struggle with precise predictions of ground snow accumulation, leading to potential economic repercussions (Winkler 2015). The variability in the settling velocity of snow particles in the atmosphere has been historically attributed to their morphology (e.g. size and shape), which poses a challenge in predicting their aerodynamic drag due to their complex and variable shapes (Locatelli & Hobbs 1974; Böhm 1989; Tagliavini *et al.* 2021*a*,*b*). Snow particle morphology is mainly determined by environmental conditions within clouds, such as temperature and humidity (i.e. supersaturation). The microphysics of ice crystal formation, extensively studied in works like Magono & Lee (1966) and Libbrecht (2005), reveals a variety of emerging crystal shapes. These range from disk-like plates and dendrites to thin-cylinder needles and columns. In conditions of high supersaturation, small, supercooled droplets can adhere to these crystals through a process known as riming, leading to the creation of sphere-like graupels. As these ice crystals fall from clouds to the ground, inter-particle collisions occur, resulting in increasingly complex particle structures such as fragments and aggregates. Besides, the interaction between air turbulence and snow particle settling has been often overlooked in simulations and laboratory experiments. Atmospheric turbulence is typically sustained by the large velocity gradients of the high-Reynolds-number atmospheric surface layer, where coherent structures across various scales emerge, and modulate the snow settling velocity (see Garrett & Yuter 2014; Nemes *et al.* 2017; Li *et al.* 2021*a*).

Historically, measurements of snow particle fall speed did not account for the influence of atmospheric turbulence. The terminal fall speed, strictly defined in quiescent flow, was directly linked to aerodynamic drag and influenced by factors like particle size, shape and mass. Various studies, including early research by Nakaya & Terada (1935), have sought to empirically correlate fall speeds with particle sizes. They observed an increase in velocity with size for graupels, crystals with droplets and needles, while noting that dendrites and powder snow typically fall at a slower rate ($\sim 0.5\,\mathrm{m\,s^{-1}}$), regardless of size. However, as their study was carried out in the laboratory setting, the snow particles might not reach their terminal velocity in a confined space. In a later study, Heymsfield (1972) introduced equations for calculating the terminal velocities of different snow morphologies, based on field measurements of drag coefficients, aspect ratios and densities. Following this, Locatelli & Hobbs (1974) developed a specialized measurement

instrument under a 3.8 m-high shielded tower, to ensure snow particles reached terminal velocity during measurement. Their extensive collection of over 300 varied snow particles led to the development of empirical equations based on dimensional power laws, each tailored to specific snow morphologies and dependent on particle size. These studies underscore the importance of size and shape in determining the varying terminal velocities of snow particles. Despite these advancements, a comprehensive understanding of the detailed settling kinematics for these diverse morphologies remains an area for further exploration.

Kajikawa's extensive research from 1976 to 1997 laid a foundational understanding of snow particle dynamics, focusing on the free-falling behaviours of various snow particle types, such as columnar snow, early snow/aggregates and plate-like snow (Kajikawa 1976, 1982, 1989, 1992; Kajikawa & Okuhara 1997). In these laboratory experiments they documented a spectrum of free-fall motions, ranging from stable, horizontal movement-free descents to more complex patterns like non-rotating glides, swings, rotating glides and spiral motions. Notably, the spiral motions exhibit inherent frequencies that correlate with the particle's Reynolds number, providing insights into the free-fall dynamics of snow particles. More systematic studies investigated the falling dynamics of idealized anisotropic particles, including disks and thin cylinders. These studies revealed that due to their large aspect ratios, such particles often orient themselves to maximize their projected area downwards during stable falls, i.e. preferential orientation. However, this steady fall is not always maintained; instabilities can lead to fluttering and even tumbling motions. These falling dynamics were explored extensively through experiments and simulations by researchers like Willmarth, Hawk & Harvey (1964), Auguste, Magnaudet & Fabre (2013) and Tinklenberg, Guala & Coletti (2023). Their work demonstrated the diverse falling styles of disks in quiescent flow, influenced by varying combinations of Reynolds number (Re) (or Galileo number, Ga; Archimedes number, Ar) and dimensionless moment of inertia (I^*). Similarly, thin cylinders, as studied by Jayaweera & Mason (1965) and Toupoint, Ern & Roig (2019), exhibit comparable settling dynamics in quiescent flow. It was observed that due to their larger aspect ratio, even minor disturbances could induce more pronounced instabilities, leading to complex spinning (rotation around the axis of symmetry) and tumbling (rotation around other axes) in these particles. These movements are important as they affect the settling of these particles through the air, potentially changing their frontal area and their drag coefficient, which in turn influences their settling velocity. As a result, particle morphology and falling styles are deeply interconnected.

Air turbulence has been observed to modulate the settling velocity and spatial distribution of heavy inertial particles, regardless of their shape, simply due to their inability to follow exactly the motion of the fluid flow around them (Maxey 1987; Wang & Maxey 1993; Yang & Lei 1998; Aliseda *et al.* 2002; Good *et al.* 2014; Falkinhoff *et al.* 2020). Most studies have focused on point particles or small spherical particles, trying to separate morphological effects from turbulence effects. As anisotropic particles already exhibit various dynamics in quiescent flow, turbulence introduces more disturbances, suggesting that the two effects can hardly be decoupled (Voth & Soldati 2017). Esteban, Shrimpton & Ganapathisubramani (2020) conducted experiments on free-falling disks and observed unique and complex settling behaviour in turbulent flows (slow tumbling and levitation). These motions displayed frequencies significantly lower than those of natural disks settling in still air. Interestingly, they noted an increase in settling velocity with greater horizontal velocity fluctuations and a decrease in oscillation frequency. Moreover, Siewert *et al.* (2014) conducted simulations on settling spheroids with various shape factors, including two extremes: disks (oblate spheroids) and needles (prolate spheroids),

under various levels of turbulence. They observed that the preferential orientation of anisotropic particles is randomized by increasing level of turbulence, thus leading to a more enhanced settling velocity (even though the morphology effect remained strong under weak turbulence).

Despite the extensive numerical simulations and laboratory experiments, there remains a notable gap in field data that capture the complexity of realistic snow particles and atmospheric flow conditions, as compared with the usage of simplified model particles (Siewert *et al.* 2014; Toupoint *et al.* 2019; Esteban *et al.* 2020; Tinklenberg *et al.* 2023) and controlled laboratory settings (Locatelli & Hobbs 1974; Kajikawa 1982, 1989, 1992; Kajikawa & Okuhara 1997). Therefore, field data are crucial for a deeper understanding of the settling dynamics of snow particles with varied morphologies in weakly turbulent conditions. Our group has been actively involved in field investigations of snow settling for the last decade. A significant advancement was the development of a super-large-scale particle image velocimetry system (SLPIV) by Hong *et al.* (2014). This system has been instrumental in visualizing flow structures in the wake of wind turbines (Hong *et al.* 2014; Dasari *et al.* 2019) and characterizing the atmospheric turbulent boundary layer (Toloui *et al.* 2014; Heisel *et al.* 2018). More recently, it has been applied to research on snow settling dynamics. Nemes *et al.* (2017) utilized this technology to quantify the settling trajectories of snow particles, measuring their Lagrangian velocity, acceleration and aerodynamic properties. Their findings revealed a significant enhancement in settling velocity due to turbulence. Building on this, Li *et al.* (2021*a*) explored snow settling and clustering under various conditions, noting clustering at near-critical Stokes numbers and an increase in settling velocity correlating with concentration and cluster size. These findings indirectly support the preferential sweeping mechanism. Furthermore, Li *et al.* (2021*b*) provided direct evidence of preferential sweeping in atmospheric turbulence by simultaneously using SLPIV and particle tracking velocimetry (PTV) for flow and snow trajectory quantification. They observed increased snow concentration and enhanced settling velocity on the downward side of vortices, directly supporting the preferential sweeping mechanism. However, these studies were limited by planar imaging, which restricts the observation of the snow particles' three-dimensional (3-D) motion, especially the spanwise motion, and did not consider the morphology effect of the snow particles. Therefore, comprehensive 3-D field investigations and simultaneous, detailed measurements of snow morphology are essential.

In this study we aim to bridge this gap by conducting field measurements during snow events using an imaging-based 3-D PTV system (Bristow *et al.* 2023) for tracking 3-D snow particle trajectories and a snow particle analyser (Li, Guala & Hong 2023) for assessing snow morphology and density. Our objectives are threefold: to understand how snow morphology influences snow aerodynamic properties, to determine the impact of morphology on particle 3-D settling kinematics and to assess how these dynamics affect snow settling velocity. Section 2 of this paper will detail the measurement instruments and data processing procedures. Section 3 will discuss the results and findings, followed by conclusions and discussions in § 4.

2. Method

We conducted a series of field experiments at the EOLOS field research station (figure 1) in Rosemount, MN, USA, spanning the winter seasons from November 2021 to April 2023. The research station is well equipped with a meteorological tower, which includes sensors for wind velocity, temperature and humidity. These instruments are crucial for assessing

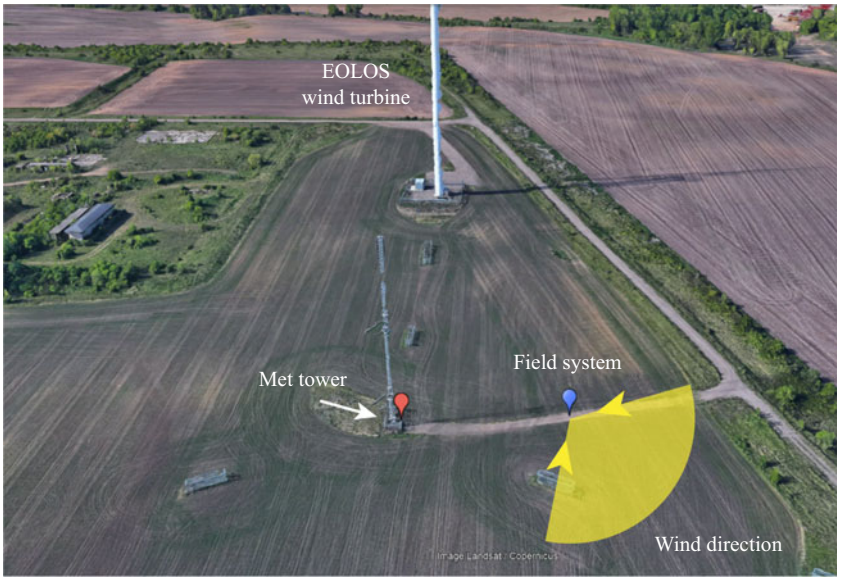

Figure 1. Aerial view of the experimental field site in Rosemount, Minnesota, retrieved from Google Maps. The annotations in the satellite image highlight the location of the system deployment and the meteorological tower, with the transparent yellow circle segment indicating the range of wind directions during the field deployments.

the atmospheric and turbulent conditions during our field experiments. The tower is fitted with four sonic anemometers (CSAT3, Campbell Scientific) at heights of 10, 30, 80 and 129 m. These anemometers, with a 20 Hz sampling rate and path lengths of 5.8 cm horizontally and 10 cm vertically, provide detailed wind velocity data. Additionally, six cup-and-vane anemometers, each with a 1 Hz sampling rate, are positioned at elevations of 7, 27, 52, 77, 102 and 126 m to complement the wind measurements. In each field deployment we utilized a 3-D PTV system, as described by Bristow *et al.* (2023), to capture the trajectories of settling snow particles. To characterize the morphology and density of these snow particles, we employed a digital inline holography (DIH) system integrated with a high-precision scale, known as a snow particle analyser, following the methodology outlined by Li *et al.* (2023).

2.1. *Experimental set-up and data processing*

Figure 2(*a*,*c*) illustrate the set-up of our 3-D PTV system. This system consists of four wire-synchronized cameras (Teledyne FLIR, FLIR Black Fly S U3-27S5C colour unit with Sony IMX429 sensor: 1464 × 1936 pixels, 4.5 μm px^{-1}) strategically positioned around a light cone 5.5 m away, spanning a 90° angle range. This light cone is created by reflecting and expanding light from a searchlight using a curved mirror, similar to the set-up used in our planar measurements. The cameras are tilted upward with 58° angles, leading them to image at a sample volume 10 m above ground. Each camera is then connected to its own data acquisition unit. These units are equipped with a board-level computer for issuing image capture commands to the cameras, a solid-state drive for storing both the system software and captured images, and a dedicated power supply. The cameras capture images with 2× decimation (732 × 968 pixels) to reach a 200 Hz frame rate. As the standard checkerboard method cannot be applied to a field of view 10 m above ground after dark

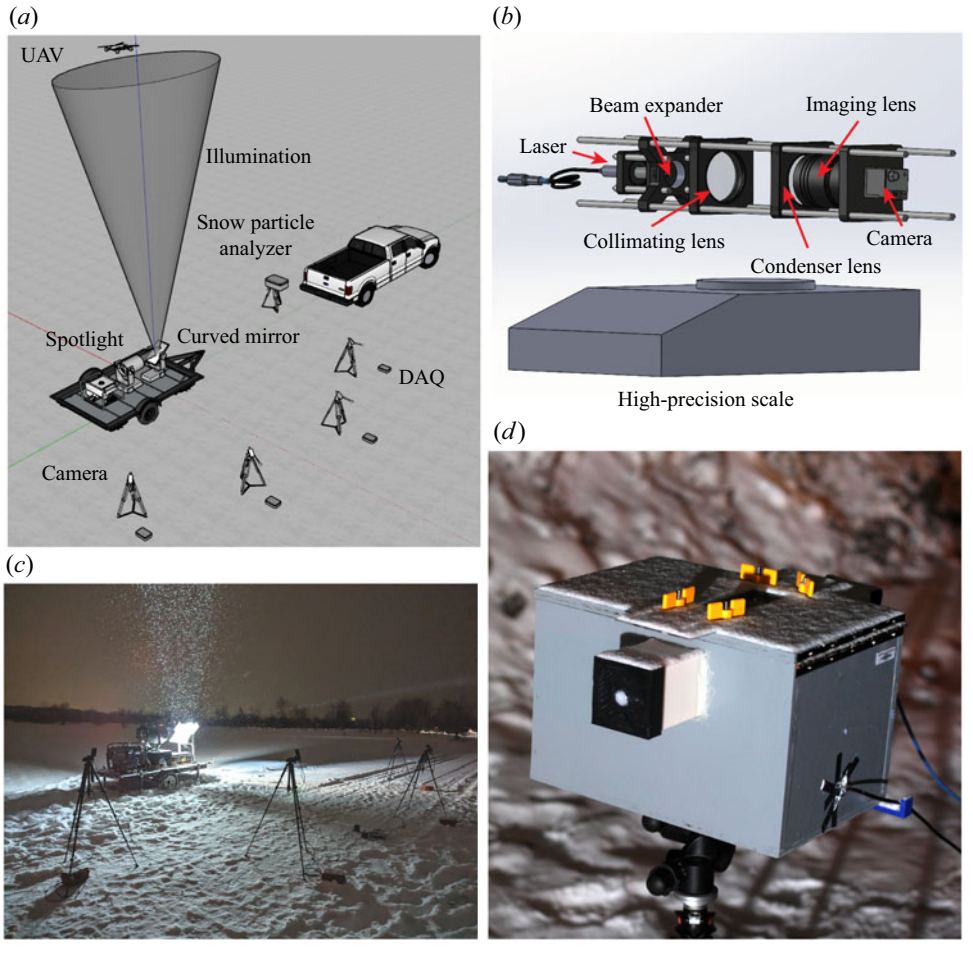

Figure 2. (*a*) Schematic depicting the field set-up for the 3-D PTV system, consisting of four cameras with their data acquisition units (DAQs), light source and an unmanned aerial vehicle (UAV) for camera calibration, together with the snow particle analyser. (*b*) Design of the snow particle analyser combining the DIH system and a high-precision scale. Actual field deployment images show (*c*) the 3-D PTV system in operation at night and (*d*) the snow particle analyser for data collection.

in the field, we use the wand calibration method described by Theriault *et al.* (2014) for camera calibration. We use two coloured light-emitting diodes (LEDs), set at a fixed distance apart on a carbon fibre rod, to act as the 'wand' attached to an unmanned drone. This calibration process is conducted multiple times before and after each deployment to ensure the same field condition between camera calibration and snow particle imaging. We have developed custom-designed camera control software that synchronizes the image capturing process across all four cameras. The calibration of the cameras is conducted using the open-access software easyWand (Theriault *et al.* 2014), which involves capturing images of the two coloured LEDs as they move within the imaging volume. The software utilizes the trajectories of the two LEDs from all four cameras to conduct the calibration, resulting in a final reprojection error within 0.25 pixels.

For tracking snow particle trajectories, we utilize an open-source implementation of the shake-the-box (STB) method (Tan *et al.* 2020). This version builds on the original STB method proposed by Schanz, Gesemann & Schröder (2016), with enhancements

specifically in the identification and removal of ghost particles. These improvements make it particularly suitable for our field data, which feature relatively high noise levels and a large field of view. This approach enables our system to capture snow particle trajectories within a considerable volume of approximately $4 \times 4 \times 6$ m^3. The system achieves a spatial resolution of 6.3 mm voxel^{-1} and a temporal resolution of 200 Hz, allowing for detailed and precise tracking of snow particle movements. The tracked snow particle trajectories are then re-oriented as a group to have the average streamwise direction as the x direction. Thus, the y direction is defined as the spanwise direction and the z direction is defined as the vertical direction. From these trajectories, we obtain the Lagrangian velocity, $\boldsymbol{u} = (u_x, u_y, u_z)$, the Lagrangian accelerations, $\boldsymbol{a} = (a_x, a_y, a_z)$ and the resulting curvature, $\kappa = \|\boldsymbol{u} \times \boldsymbol{a}\|/\|\boldsymbol{u}\|^3$, where $\times$ represents the cross-product. We use the second-order central difference method to calculate the Lagrangian velocity (first-order derivative) and acceleration (second-order derivative). The approximation introduces an inherent error, $O(\Delta t^2)$, which depends directly on the time step and is relatively small. However, the positioning errors of the snow particles can propagate and magnify in the velocity and acceleration calculation. As discussed by Schanz *et al.* (2016) and Tan *et al.* (2020), the iterative particle reconstruction, STB tracking and trajectory filtering techniques significantly refine and reduce positioning errors. We quantify the root mean square of the difference between trajectory positions before and after filtering to be 0.3 pixels. This reduction potentially compensates for the positioning errors inherited from camera calibration, resulting in smaller errors in velocity and acceleration calculations. Consequently, the actual uncertainties in measuring velocity and acceleration are primarily influenced by the selection of the filter length, which ranges from 45 ± 2 frames (see Appendix A). This leads to an average acceleration uncertainty of 0.34 m s^{-2}.

To complement our 3-D PTV system, we also deployed a snow particle analyser near the 3-D PTV set-up to assess the morphology and density of snow particles during each snow event (figure 2*b*,*d*). All these measurements are crucial for accurately estimating the terminal velocity of snow particles in still air. As shown in figure 2(*c*), the snow particle analyser employs a DIH system, which captures holograms of snow particles within a sample volume of $2.9 \times 2.2 \times 14.0$ cm^3. This system achieves a spatial resolution of 14 μm pixel^{-1} and a temporal resolution of 50 Hz. Through image analysis of the holograms, we obtain detailed information on particle size and shape, specifically the area equivalent diameter (D_{eq}), major axis length (D_{maj}), minor axis length (D_{min}), area (A_e), etc. We also classify the shape of each particle into one of six types: aggregates, graupels, dendrites, plates, needles and small particles. We define the characteristic particle size (D_p) as the area equivalent diameter for aggregates, graupels and small particles, and as the major axis length for dendrites, plates and needles. Additionally, a high-precision scale measures the weight of snow particles passing through the DIH sample volume, allowing us to estimate the average density of the particles. We also perform conditional sampling to achieve measurement of the density of individual snow particles.

For estimating the aerodynamic properties of snow particles, we follow the method proposed by Böhm (1989). This method involves calculating the Best number X (also known as the Davies number), a dimensionless number that incorporates only the physical properties of snow particles and ambient air, and represents the equilibrium between gravity and drag forces. The Best number is defined as

$$X = C_D Re_p^2 = \frac{8\rho_p V_p g \rho_a}{\pi \mu^2} \left(\frac{A}{A_e}\right)^{1/4}. \tag{2.1}$$

Noteworthily, unlike particle Reynolds number ($Re_p = \rho_a W_0 D_p/\mu$) and drag coefficient ($C_D$), the definition of the Best number eliminates the need to incorporate particle terminal velocity in the formulation, which is not readily available for complex snow particles. In (2.1), ρ_p and V_p are the density and volume of the snow particles, respectively, which are specific to the type of snow particle, as detailed in Li *et al.* (2023). Specifically, we approximate the complex snow particles as spheroids (graupels and small particles), combinations of small spheroids (aggregates), disks with thickness in correlation with their diameter (plates and dendrites) and thin cylinders (needles and columns). Such a method minimizes errors in volume estimation as compared with the typical spherical assumption used in the snow measurement community, resulting in the uncertainties of the volume estimation within 10 % for snow particles with irregular shape (aggregates) and uncertainties of density within 20 % for all demonstration cases in Li *et al.* (2023). Here A_e is the effective snow particle imaged area, and A is the circumscribed area of the enclosing circle or ellipse. Such an area ratio, A/A_e, serves as a simplified two-dimensional (2-D) measure of porosity and is instrumental in better predicting the drag of complex snow particles. As the snow morphological parameters are quantified by the snow particle analyser while particles settle in various orientations, we assume that the ratio A/A_e remains constant regardless of orientation. Finally, ρ_a and μ are the density and viscosity of air, respectively.

Following the definition of the Best number, the drag coefficient of snow particles is modelled as a function of the particle Reynolds number, accounting for the unique morphology of snow particles. This approach indirectly incorporates the effect of snow particle density, which contributes to increasing the settling velocity. According to Stokes' law for $Re_p \sim O(1)$, the correlation for the drag coefficient dependent on the particle Reynolds number is $C_D = 24/Re_p$. However, the Stokes' law becomes invalid as the Reynolds number increases, especially for complex snow particles. Researchers have made various attempts to model the drag coefficient of snow particles theoretically (Böhm 1989; Khvorostyanov & Curry 2002, 2005; Mitchell & Heymsfield 2005). As suggested by Böhm (1989) and references therein, the drag coefficient of snow particles is modelled by considering the boundary layer surrounding the snow particles as a whole:

$$C_D = C_0 \left(1 + \frac{\delta_0}{Re_p^{1/2}}\right)^2. \tag{2.2}$$

Here $C_0 = 0.6$ is an inviscid drag coefficient and $\delta_0 = 5.83$ is a parameter controlling the evolution of the particle boundary layer, likely depending on the particle surface roughness, both empirically estimated. Equation (2.2) has the form of corrected Stokesian drag for a rigid sphere (Kaskas 1970), but with different coefficients, modulating the transition from a linear drag at low Re_p to a constant drag coefficient C_0 in the Re_p independent regime. The effect of different snow morphologies is included in the A/A_e term in (2.1), which is then used to predict the snow type specific drag coefficients, $C_{De} = (A/A_e)^{3/4} C_D$. The C_0 and δ_0 parameters have been more recently updated, along with the dependency on the area ratio, by Heymsfield & Westbrook (2010) and McCorquodale & Westbrook (2021). Additional corrections considering turbulent boundary layer, temperature, humidity and accounting for different snow particle types, have been discussed in Khvorostyanov & Curry (2002, 2005) and Mitchell & Heymsfield (2005).

As described in Böhm (1989), we then obtain a semi-analytical and semi-empirical equation for the particle Reynolds number by combining (2.1) and (2.2):

$$Re_p = \frac{\delta_0^2}{4}\left(\left(1+\frac{4X^{1/2}}{\delta_0^2 C_0^{1/2}}\right)^{1/2}-1\right)^2. \tag{2.3}$$

The terminal velocity of the snow particles (W_0) in quiescent air is then calculated from the Reynolds number, $Re_p = \rho_a W_0 D_p/\mu$. Once the terminal velocity is obtained, the aerodynamic particle response time is defined as $\tau_p = W_0/g$.

The analyses described have been meticulously applied to each snow particle type, leveraging the unique physical properties of individual particles, captured by the snow particle analyser. Through a detailed examination of the collected holograms, we identify and classify each particle, subsequently analysing their specific inertial properties, namely D_p, ρ_p, A and A_e. By employing these properties within the Böhm model (Böhm 1989), we were able to estimate the aerodynamic properties of each particle. This rigorous method allows us to calculate the distribution and mean values of the terminal velocity (W_0) and drag coefficient for individual snow particles and specific snow types.

2.2. *Turbulence and snow conditions in the field*

Over the course of the winter seasons from December 2021 to April 2023, we successfully carried out eight field deployments, encompassing a diverse range of environmental conditions. These deployments allowed us to study four major types of snow particles: aggregates, graupels, dendrites/plates and needles/columns. We encountered wind speeds varying from a gentle $0.6\,\mathrm{m\,s^{-1}}$ to a more intense $8.4\,\mathrm{m\,s^{-1}}$. Based on these wind speeds, we categorized the conditions into three turbulence levels: weak turbulence (wind speed less than $3\,\mathrm{m\,s^{-1}}$ with turbulent kinetic energy (TKE) below $0.3\ \mathrm{m^2\ s^{-2}}$), moderate turbulence (wind speed between 3 and $6\,\mathrm{m\,s^{-1}}$ with TKE ranging from 0.3 to $2.0\ \mathrm{m^2\ s^{-2}}$) and relatively strong turbulence (wind speed exceeding $6\,\mathrm{m\,s^{-1}}$ with TKE above $2.0\ \mathrm{m^2\ s^{-2}}$). These turbulent properties were measured using the sonic anemometer positioned at a height of 10 m. Details of the estimation methods of these quantities can be found in Li *et al.* (2021*b*). We use the second-order structure function of the streamwise velocity fluctuation to estimate the dissipation rate (ε). The Taylor microscale (λ) is then calculated as $\lambda = u'\sqrt{15\nu/\varepsilon}$, where $u' = \sqrt{(u_x'^2 + u_y'^2 + u_z'^2)/3}$ is the representative scale of fluctuating velocity and ν is the viscosity of air. Given the variety of snow particle types and wind speeds, our field data encompasses a total of 31 distinct conditions. To effectively separate the influences of snow morphology and atmospheric turbulence on snow settling velocity, a more systematic classification of the field snow and turbulence conditions is essential. We propose using the settling parameter $Sv_L = W_0/u'$, which quantifies the relative impact of turbulence on snow gravitational settling (Petersen, Baker & Coletti 2019; Brandt & Coletti 2022). This parameter represents the ratio of the snow particle's terminal velocity in still air (W_0) to the root mean square of the turbulent velocity fluctuations (u'). A higher value of Sv_L indicates that the influence of turbulence on the snow settling velocity is relatively minor.

In our analysis, we utilized the settling parameter, wind speed and TKE as key criteria to categorize our 3-D PTV and snow particle analyser datasets. This approach led us to identify four distinct groups, which we labelled as 'weak turbulence' cases, with relatively smaller Taylor Reynolds number (Re_λ) and higher settling parameters (Sv_L) as shown in

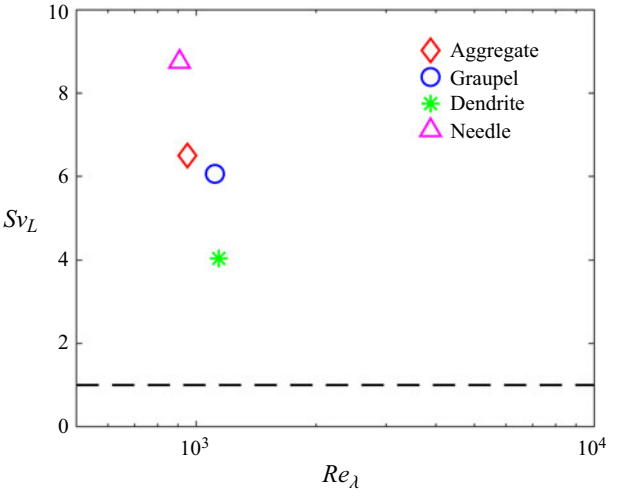

Figure 3. A summary of the Taylor Reynolds number of the atmospheric flow (Re_λ) and settling parameter of the snow particles (Sv_L) for different snow particle types. Data points for aggregates are marked with a red diamond, graupel with a blue circle, dendrites with a green star and needles with a magenta triangle.

figure 3. We assess the turbulence and micro-meteorological conditions for each group detailed in table 1, employing estimation methods as outlined in the studies by Nemes *et al.* (2017) and Li *et al.* (2021*b*). Each group is dominated by one specific type of snow particle, which constitutes more than half of the snow population in the dataset. These types are aggregates, graupels, dendrites and needles, as detailed in table 2 and illustrated in the size and shape distributions in figure 4. We leverage the capabilities of the snow particle analyser, as detailed in § 2.1, to estimate these physical properties of snow particles. During a selected one-hour period characterized by dominant snow particle types, our analysis encompasses 200 000 holograms for each type of snow particle. This comprehensive dataset yields detailed information about approximately 28 000 aggregates, 13 000 graupels, 30 000 dendrites and 21 000 needles. Complementing the snow particle analyser measurements, our 3-D PTV datasets include a total of 500 s of images for each dominant snow type, which are broken down into 50 s segments throughout the one-hour period selected. This rich dataset facilitates the identification of millions of snow particle trajectories, specifically around 322 000 for aggregates, 285 000 for graupels, 1 037 000 for dendrites and 182 000 for needles, providing orders of magnitude more data than our previous studies. Specifically, our 3-D PTV system measures the complete 3-D velocity and particle acceleration components. The additional spanwise dimension of the data, compared with planar measurements, enables a thorough analysis of snow particle kinematics, including trajectory curvature and meandering. Furthermore, the integration of the 3-D PTV system with the snow particle analyser allows us to correlate the specific morphology of snow particles (e.g. size, shape and type) with their settling behaviour.

For the detected snow particles, their size and shape are measured through image analysis described in § 2.1. Given that these particles may present various orientations relative to the imaging plane, relying solely on the projected area (or equivalent diameter) falls short of providing a precise representation of the characteristic size of each particle, especially the non-spherical ones. We thus define the particle size as the equivalent diameter for aggregates and graupels, the major axis for dendrites (diameter) and needles (length), as detailed in Li *et al.* (2023). Upon closer examination, we observed notable

https://doi.org/10.1017/jfm.2024.601 Published online by Cambridge University Press

Dataset	U (m s^{-1})	$u_{x,rms}$ (m s^{-1})	$u_{y,rms}$ (m s^{-1})	$u_{z,rms}$ (m s^{-1})	TKE (m^2 s^{-2})	L (m)	τ_L (s)	ε (cm^2 s^{-3})	η (mm)	τ_η (s)	λ (mm)	Re_λ (–)	T (°C)	RH (%)
Aggregate	1.30	0.19	0.17	0.11	0.05	2.5	13	2.3	1.8	0.24	179	950	−4	95
Graupel	1.26	0.20	0.19	0.16	0.06	3.1	15	2.8	1.7	0.22	172	1114	−10	87
Dendrite	1.69	0.30	0.27	0.19	0.14	2.4	8	9.2	1.3	0.12	138	1139	0.4	96
Needle	1.30	0.19	0.17	0.11	0.05	2.5	13	2.3	1.8	0.24	179	908	−4	95

Table 1. Overview of atmospheric turbulence parameters across datasets, detailing wind speed, turbulence fluctuations, turbulence kinetic energy (TKE), integral scale (L), dissipation rate (ϵ), Kolmogorov scale (η), Taylor microscale (λ), Reynolds number ($Re_\lambda = \lambda u_{x,rms}/\nu$), ambient temperature ($T$) and relative humidity (RH).

Snow type	Aggregate (%)	Graupel (%)	Dendrite (%)	Needle (%)	$\overline{D_p}$ (mm)	$\overline{D_{min}/D_{maj}}$ (–)	$\overline{A/A_e}$ (–)	$\overline{\rho_p}$ (kg m^{-3})
Aggregate	55.8	21.1	14.0	9.1	0.96 ± 0.63	0.61 ± 0.19	1.22	90
Graupel	2.5	93.3	3.7	0.5	0.75 ± 0.28	0.80 ± 0.16	1.06	220
Dendrite	16.9	19.3	55.4	8.4	0.93 ± 0.66	0.58 ± 0.21	1.98	280
Needle	13.2	22.4	7.2	57.2	0.74 ± 0.34	0.58 ± 0.20	1.21	360

Table 2. Comparative overview of snow particle characteristics across various dataset groups, including the proportion of snow types where the dominant type exceeds 50% occurrence, the mean diameter (defined as the average equivalent diameter for aggregates and graupels, as well as the average major axis length for dendrites and needles), aspect ratio, area ratio and density values characterizing each dataset group.

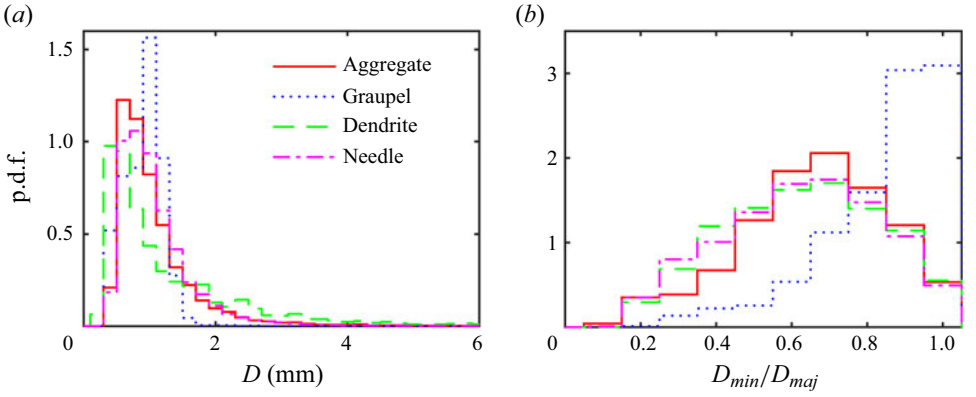

Figure 4. (*a*) Probability distribution functions (p.d.f.s) of snow particle size (D_p, defined as the equivalent diameter for aggregates and graupels, as well as the major axis length for dendrites and needles) and (*b*) p.d.f.s of the aspect ratio (D_{min}/D_{maj}) for various snow types, plotted with different line styles and colours: aggregates are represented by red solid lines, graupel by blue dotted lines, dendrites by green dashed lines and needles by magenta dash-dotted lines.

differences among these types. Graupels and needles, for instance, tend to have a more uniform size distribution, with a smaller average size and standard deviation compared with aggregates and dendrites. Aggregates and dendrites, on the other hand, are generally larger, and their datasets include a mix of other particle types, resulting in a broader size distribution. We also analysed the aspect ratio (i.e. the ratio between the minor and major axes lengths, D_{min}/D_{maj}) of these snow particles, defined as the ratio of their minor to major axis lengths, as measured by the snow particle analyser. Graupels predominantly exhibit aspect ratios greater than 0.8, indicating their near-spherical shape. In contrast, the aspect ratios for the other types vary significantly from one, suggesting more anisotropic shapes. In this respect, note that the 2-D holograms do not allow us to accurately capture the averaged thickness of plate-like crystals due to the random particle orientation, unless further analysis is performed on selected particle images as in Li *et al.* (2023). Furthermore, we measured the average density ($\overline{\rho_p}$), together with the average particle size ($\overline{D_p}$) and aspect ratio ($\overline{D_{min}/D_{maj}}$), of the four datasets using the snow particle analyser. Needles, being solid crystals with minimal riming, have the highest average density of 360 kg m^{-3}. Dendrites follow with an average density of 280 kg m^{-3}, as it is influenced by the gaps between branches, which contribute to the overall porosity of the particles. Graupels have an average density of around 220 kg m^{-3}, aligning with

our previous measurements. Moreover, aggregates exhibit the lowest density of around 90 kg m^{-3}, as expected, attributable to their larger size and higher porosity.

3. Results

Utilizing the snow particle analyser, we have successfully measured both the morphology and density of snow particles, enabling us to accurately predict their aerodynamic properties. Additionally, our 3-D PTV system has provided detailed 3-D settling dynamics from millions of snow particle trajectories. Armed with this comprehensive data, we address three key questions in the following section. First, how does the morphology of snow particles influence their aerodynamic properties? Second, in what ways does morphology impact the settling kinematics of these particles? Third, how do the varying settling dynamics among different types of snow particles affect the overall settling velocity of snow? These inquiries form the core of our investigation, shedding light on the intricate interplay between snow particle morphology and their settling behaviour through the atmosphere.

3.1. *Aerodynamic properties*

This section presents an in-depth examination of the aerodynamic characteristics, including their terminal velocity, drag coefficient and settling velocity, for each snow particle type. Table 3 consolidates key aerodynamic parameters derived from our analysis: the average settling velocity ($\overline{W_s}$) obtained through 3-D PTV, the average estimated still-air terminal velocity ($\overline{W_0}$) as outlined in § 2.1, the velocity fluctuation (u') and the Kolmogorov time scale (τ_η) of the flow, the particle's Stokes number ($St_\eta = \tau_p/\tau_\eta$), their settling parameter ($Sv_L = \overline{W_0}/u'$) and the Froude number ($Fr_\eta = a_\eta/g$, where $a_\eta = u_\eta/\tau_\eta$ is the Kolmogorov scale acceleration). Needles exhibit the highest terminal velocity among all four types. With the same particle size, the cylindrical-shaped needles have the smallest projected area and the highest density, leading to larger terminal velocities. The Stokes number gauges the particle's velocity response to sudden changes in flow, with values around one signifying a critical condition for turbulence–particle interactions. Settling parameters greater than one imply a weak influence of turbulence on the settling particles. The Froude number, a ratio of the characteristic flow acceleration ($a_\eta = u_\eta/\tau_\eta$) to gravitational acceleration, suggests that gravitational settling is more pronounced than the turbulence effect on the particles (Bec, Homann & Ray 2014). Comparatively, the settling velocity enhancements from the terminal velocities are moderate, ranging up to 32 % for aggregates, 13 % for dendrites, 4 % for needles and 3 % for graupels. These findings indicate that the turbulence effects (e.g. preferential sweeping and loitering) on particle settling is generally weak under the examined conditions. Variations in settling enhancement across snow types may be largely attributable to differences in particle size, shape and density.

Figure 5 presents a comparative analysis of the probability density functions (p.d.f.s) for settling velocity (W_s) and estimated still-air terminal velocity (W_0) across various snow particle types. The estimate of W_0 is based on the Best number, $X = C_D Re_p^2$, which does not directly depend on the settling velocity of the snow particles, but rather on their physical properties and the ambient air. Following the approach of Böhm (1989), summarized by (2.1)–(2.3), we estimate the terminal velocity from measurable geometric and inertial properties by the snow particle analyser. The p.d.f.s for graupel, which are nearly spherical in shape, exhibit a close overlap between the settling and terminal velocities, indicating a minimal influence of turbulent eddies on their settling dynamics.

Snow type	$\overline{W_s}$ (m s^{-1})	$\overline{W_0}$ (m s^{-1})	u' (m s^{-1})	τ_η (s)	St_η (–)	Sv_L (–)	Fr_η (–)
Aggregate	1.37 ± 0.22	1.04 ± 0.31	0.16	0.238	0.44	6.5	0.003
Graupel	1.06 ± 0.25	1.03 ± 0.34	0.17	0.218	0.48	6.0	0.006
Dendrite	1.14 ± 0.24	1.01 ± 0.60	0.25	0.119	0.87	4.0	0.009
Needle	1.45 ± 0.17	1.40 ± 0.66	0.16	0.238	0.60	8.7	0.003

Table 3. Summary of characteristic parameters for snow particles and atmospheric flow, encompassing average terminal ($\overline{W_0}$) and settling velocities ($\overline{W_s}$), Stokes number (St_η), settling parameter (Sv_L), flow velocity scale (u'), Kolmogorov time scale (τ_η) and Froude number (Fr_η).

Note that the 'dent' in the distribution of the terminal velocity of graupels in figure 5(*b*) reflects their size distribution. On the contrary, for the other snow types – characterized by non-spherical geometries – the p.d.f.s diverge despite the mean settling and terminal velocities for needles displaying only a 4 % discrepancy. This variation suggests that the aerodynamic behaviour of non-spherical particles is considerably affected by the randomization of their orientation due to flow disturbances and unsteady behaviour. In quiescent conditions, particles falling stably tend to orient themselves to maximize the aerodynamic drag (i.e. preferential orientation), potentially due to the inertial forces of the surrounding media, presenting their maximal cross-sectional area perpendicular to the fall direction (Willmarth *et al.* 1964; Cho, Iribarne & Richards 1981). However, in turbulent conditions, such a preferential orientation is not appreciable (Cho *et al.* 1981; Klett 1995), and the varying orientations result in a reduced effective cross-sectional area, potentially leading to an increased average settling velocity for non-spherical particles. Furthermore, while the settling velocity distributions for different snow types approximate a Gaussian profile, the estimated terminal velocities are rather skewed. This asymmetry arises from the inherent size distributions of the snow particles, which are typically modelled using a gamma distribution (Field, Heymsfield & Bansemer 2007). We also acknowledge the potential sampling differences between the 3-D PTV measurements (likely under-representing the finest size fraction) and the snow particle analyser data collection.

Historical studies have demonstrated that the terminal velocity of snow particles exhibits a size-dependent characteristic, since the early research by Nakaya & Terada (1935), Heymsfield (1972) and Locatelli & Hobbs (1974) fitting empirical data to establish a particle-mass-based approach to the settling. Specifically, Locatelli & Hobbs (1974) conducted a thorough investigation of various snow particle types, deriving power-law empirical formulas to represent the size-dependent terminal velocity, expressed as $W_0 = aD_p^b$, where a and b are constants that differ based on the snow particle type, based on shape and density. For our analysis, we employed the formulas relevant to aggregates of unrimed radiating assemblages of dendrite ($W_0 = 0.8D_p^{0.16}$), conical graupel ($W_0 = 1.2D_p^{0.65}$), rimed dendrites ($W_0 = 0.62D_p^{0.33}$) and rimed columns ($W_0 = 1.1L^{0.56}$, where L is the length). Such power-law equations can be empirically obtained by fitting the size distributions in figure 4 with the settling velocity in figure 5. We optimize the linear coefficient with the same exponent to impose the same mean and similar distribution of the settling velocity for each snow type and, thus, obtained the empirical equations: $W_s = 1.45D_p^{0.16}$ for aggregates, $W_s = 1.2D_p^{0.65}$ for graupels, $W_s = 0.92D_p^{0.33}$ for dendrites, $W_s = 1.66L^{0.56}$ for needles. We thus obtain the same equation for W_0 and W_s for graupels, suggesting close alignment in the mean values and distributions between the

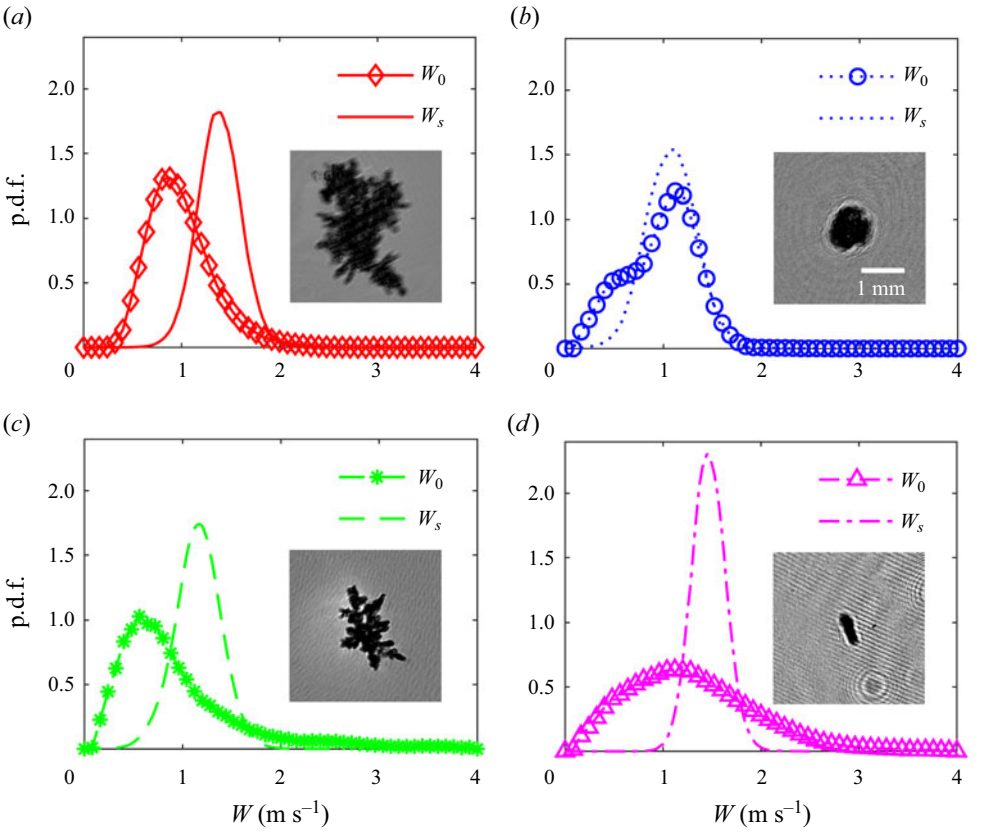

Figure 5. Probability distribution functions (p.d.f.s) contrasting the estimated still-air terminal velocity (W_0) using snow properties measured by the snow particle analyser and the experimentally measured settling velocity (W_s) by the 3-D PTV system for four datasets with different dominant snow types: (*a*) aggregates, (*b*) graupel, (*c*) dendrites and (*d*) needles. Insets within each panel display representative holographic images of the corresponding snow particle type.

measured settling velocities and the estimated terminal velocities, the same as predicted using equations from Böhm (1989). This also confirms negligible effects by the specific atmospheric turbulence conditions monitored during the settling of graupels. In contrast, for other non-spherical types of snow, the linear coefficients for W_s are higher than those of W_0. This discrepancy highlights the morphology effects that modulate the settling velocity of these non-spherical snow particles, with potential turbulence effects considering the varying particle orientation because of turbulence disturbances, and the production of the Stokes number and settling parameter reaching critical condition ($St_\eta Sv_L \sim 1$, as suggested in Petersen *et al.* 2019; Brandt & Coletti 2022).

To better model the terminal velocity, it is important to quantify the aerodynamic drag of snow particles for various morphological types. In figure 6 we present the mean drag coefficients and mean Reynolds numbers, estimated using the average particle size and measured settling velocity. The error bars indicate the variability of these quantities, reflecting the distribution of snow particle sizes and settling velocities as represented by their standard deviations. The drag coefficient is calculated as $C_{De,mean} = 2\overline{\rho_p}\overline{V_p}g/(\rho_a\overline{W_s^2}\overline{A_{e,max}})$, where $\overline{\rho_p}$ is the average snow particle density, $\overline{V_p}$ is the average particle volume (different expressions for different snow particle types defined in Li *et al.*

2023), $\overline{W_s^2}$ is the mean square settling velocity and $\overline{A_{e,max}}$ is the average maximal projected area of the measured snow particles (e.g. a flat-falling dendrite, see Appendix B). The snow particles have an average Reynolds number ($Re_{p,mean} = \overline{W_s}\ \overline{D_p}/\nu$) of the order of 100, agreeing with typical field measurements (Heymsfield & Westbrook 2010). The drag coefficients for aggregates, graupels and needles agree well with the model predictions from Böhm (1989, equation (2.2)), $C_{De} = (\overline{A/A_e})^{3/4} C_0(1 + \delta_0/Re_p^{1/2})^2$, as presented by the dotted lines. Note that the average area ratio, $\overline{A/A_e}$, is calculated from the snow particle holograms for each snow type, and it is necessary to rescale the generalized drag equation (2.2) to the specific snow morphologies (Böhm 1989). As graupels show more sphere-like features, their drag coefficient leans towards that of spheres (corrected for high Reynolds number by Kaskas 1970). Despite the smaller terminal velocity for the non-spherical particles considering the particle orientation, the drag coefficient is well predicted by the Böhm (1989) model for aggregates and needles. Potential contamination from other types (∼20 % after filtering out particles with close to an aspect ratio of 1) within the datasets might lead to the mismatch between the p.d.f.s of the terminal velocity and measured settling velocity for needles. The enhanced settling for aggregates could be a combined result of particle orientation, weak turbulence enhancement considering the critical condition of $St_\eta Sv_L \sim 1$ and contamination from other types that do not align with the statistically dominant group, as shown in table 2. Moreover, the dendrites show, on average, a higher drag coefficient as compared with the other types, potentially due to their large frontal area and higher density. Such a discrepancy could also explain the underestimation of the terminal velocity of dendrites by the equations from Böhm (1989), considering the higher, on average, settling velocity. The error bars in figure 6 represent the natural variability of the data sample rather than measurement errors. However, measurements taken using the 3-D PTV system and snow particle analyser do introduce errors in settling velocity, particle volume and density estimates. Based on Appendix A, the velocity measurement uncertainty is estimated to be $0.002\,\mathrm{m\,s^{-1}}$. From our previous study (Li *et al.* 2023), the volume estimation uncertainty is around 5% due to size measurement and classification errors, leading to a similar 5 % uncertainty in density estimates. Since the drag coefficient depends on particle size, density and settling velocity, we estimate the overall measurement error for C_D to be approximately 7.4 %, while the error for Re_p is around 2.2 %. Additional errors may arise due to the presence of other snow morphologies during the investigated periods. By selecting only the snow particles matching the dominant snow types – aggregates and dendrites – while maintaining the estimated average density and the measured averaged velocity, we calculated C_D and Re_p values as 1.9 and 139 for aggregates, compared with 1.6 and 108 when including all snow particle types within the aggregate-dominant dataset. For dendrites, the calculation yielded a higher drag coefficient of 4.4, compared with 3.6 when all snow particles were considered, with the particle Reynolds number around 166, compared with 90. All the above estimated measurement errors lead to uncertainties in the quantities that are within the plotted standard deviations represented in figure 6. We further compare our measurements with laboratory experiments by Tagliavini *et al.* (2021*a*), with squares representing the aggregates (AgCr77, Ag15P1, AgSt18), pentagrams representing the dendrite (D1007) and left-pointed triangles representing the columnar snow (CC20Hex2). Our measurements agree well with the laboratory experiments, with the dendrite type showing a larger drag coefficient due to its disk-like shape. Such observations provide insights for snow settling modelling, especially for the predominantly dendrite snow events, as they show a large deviation from the Böhm (1989) model prediction.

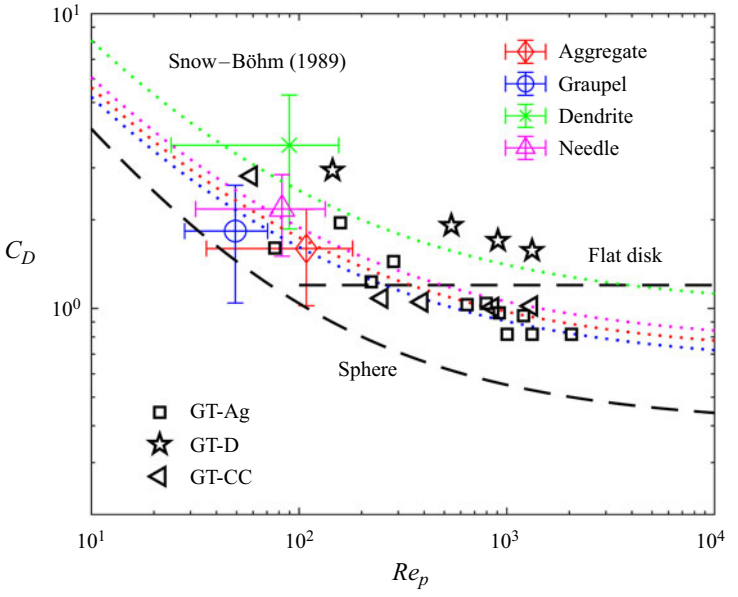

Figure 6. The relationship between drag coefficient (C_D) and particle Reynolds number (Re_p) for four types of snow particles. Presented data points, with corresponding error bars indicating the natural variability in the data sample, denote mean values of C_D and Re_p derived from average particle size and settling velocity for each snow type: aggregates (red diamond), graupel (blue circle), dendrites (green star) and needles (magenta triangle). These measured data are compared against theoretical $C_D - Re_p$ correlations for spheres (dashed line, Kaskas 1970) and flat disks at high Re_p values Roos & Willmarth (1971), as well as with empirical correlation ($C_{De} = (\overline{A/A_e})^{3/4} C_0 (1 + \delta_0 / Re_p^{1/2})^2$) for natural snow particles (dotted lines, with the same colour scheme as the measured drag coefficient) and recent findings from 3-D-printed snow particles (black squares, pentagrams and left-pointed triangles) by Tagliavini *et al.* (2021*a*).

3.2. *Settling kinematics*

3.2.1. *Qualitative observation*

Besides the settling velocity, the kinematic behaviours of snow particle settling trajectories are as variable as their shapes, with morphology playing a significant role in their settling behaviour. Similar to the findings of Kajikawa's laboratory studies (Kajikawa 1976, 1982, 1989, 1992; Kajikawa & Okuhara 1997), snow particles demonstrate a range of falling styles under weak atmospheric turbulence, akin to those of disks and thin cylinders in quiescent flows. Figure 7 displays a collection of snow particle trajectories, differentiated by the colour-coded spanwise acceleration, from datasets dominated by different snow types. The distinct kinematics observed here are likely a consequence of each type's unique morphology under similar atmospheric conditions. Aggregates and dendrites, in particular, exhibit a pronounced meandering motion, characterized by substantial acceleration fluctuations at a relatively low frequency. This behaviour could be attributed to their larger sizes and frontal areas, which, when subject to even weak atmospheric turbulence, result in unstable settling patterns marked by fluttering or tumbling motions. In contrast, graupels, with their quasi-spherical form, show a relatively high-frequency, low-magnitude meandering motion, and maintain a consistent travel direction. This suggests that graupels can better follow the fluid flow, considering their smaller particle size and lower density compared with the other non-spherical particle types, with their meandering motion possibly revealing interactions with small turbulent

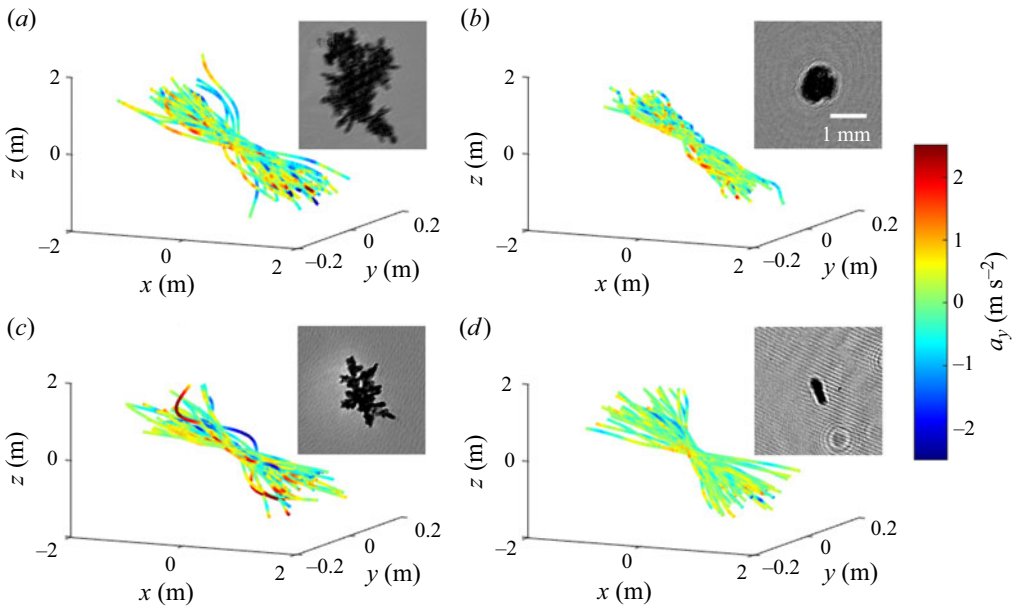

Figure 7. A random selection of 50 trajectories for four snow particle types, with paths colour coded according to spanwise acceleration and centred at the origin. Panels (*a–d*) each display a group of sample trajectories for (*a*) aggregates, (*b*) graupel, (*c*) dendrite and (*d*) needles. Insets provide corresponding holograms for each snow type. We remind the reader that with our coordinate system aligned with the mean wind direction, all particles will travel towards a positive x value.

eddies. Needles exhibit weak magnitude and infrequent fluctuations in acceleration, but appear to experience a wider spanwise velocity range, as shown by the spread of trajectories in the spanwise direction. Their elongated, cylindrical shape, presenting a minimal frontal area relative to length, likely contributes to their tendency to align with the flow, resulting in this distinct settling pattern. Additionally, a detailed but qualitative examination of the trajectories indicates that non-spherical particles predominantly exhibit zig-zag motions, potentially due to the vortex shedding in their wake (Willmarth *et al.* 1964; Toupoint *et al.* 2019), whereas graupels tend to follow more helical paths, potentially spiralling around vortex tubes (Mezić, Leonard & Wiggins 1998).

3.2.2. *Kinematic quantification*

To thoroughly analyse the kinematics of snow particles, we examine their trajectories using the particle velocity ($\boldsymbol{u} = (u_x, u_y, u_z)$), the Lagrangian accelerations ($\boldsymbol{a} = (a_x, a_y, a_z)$) and the resulting curvature ($\kappa = \|\boldsymbol{u} \times \boldsymbol{a}\|/\|\boldsymbol{u}\|^3$), where $\times$ represents the cross-product. The curvature quantifies the trajectory's deviation from a straight path, influenced by flow structures or the snow particle morphology. We define two curvatures: one based on the original path and another adjusted to reduce the effect of the different mean streamwise flow and settling velocities across datasets ($\kappa = \|\boldsymbol{u}' \times \boldsymbol{a}\|/\|\boldsymbol{u}'\|^3$, with $\boldsymbol{u}' = (u_x - \overline{u_x}, u_y, u_z - \overline{u_z})$). Figure 8 demonstrates this analysis with the trajectory of a dendrite snow particle. The apparent sinusoidal meandering is an actual measurement from our 3-D PTV system. This meandering is underscored by the sinusoidal patterns in the velocity and acceleration components (figure 8*b*,*d*), particularly pronounced in the acceleration signals in the horizontal plane. Spectral analysis of the acceleration variation along specific trajectories enables us to discern the strength and frequency of the meandering motion

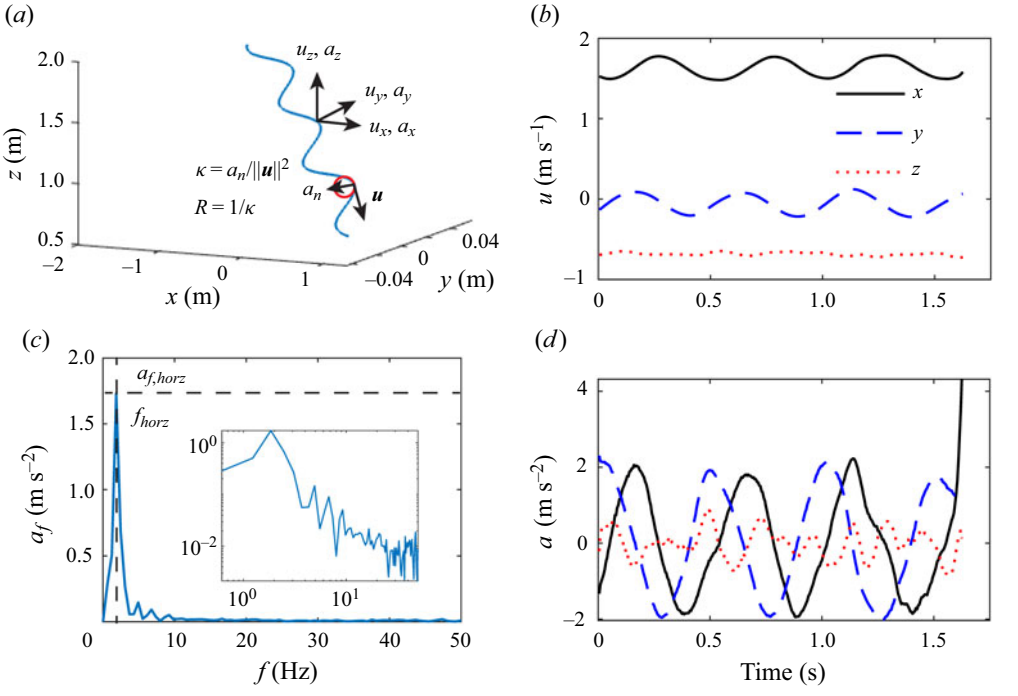

Figure 8. Kinematic analysis of a sample trajectory. (*a*) Annotated meandering trajectory of a dendrite snow particle detailing its Lagrangian velocity components (u_x, u_y, u_z), accelerations (a_x, a_y, a_z), curvature (κ) and radius of curvature (R). (*b*) Temporal variations in the three velocity components along the trajectory: x (black solid line), y (blue dashed line), z (red dotted line). (*c*) Frequency spectrum of horizontal acceleration, highlighting the peak frequency and maximum fluctuation amplitude. Inset shows the same spectrum in log-log scale. (*d*) Corresponding temporal variations in the three acceleration components along the trajectory with the same colour scheme as in (*b*).

(figure 8*c*). The dominant frequency is identified from the spectral peak, and the intensity is characterized by the magnitude of the horizontal acceleration fluctuations at this frequency. This comprehensive analysis yields detailed insights into how the morphology of snow particles influences their settling dynamics, particularly highlighting the effects on their acceleration statistics and trajectory geometry, which will be explored in depth in subsequent sections.

3.2.3. *Acceleration statistics*

Having quantified the settling trajectories of snow particles, we proceed to examine and compare the acceleration statistics across datasets featuring four snow particle types. Figure 9 presents a detailed comparison of the acceleration behaviours of different types through the normalized acceleration p.d.f.s and the Lagrangian acceleration autocorrelation. The acceleration response of the particles is influenced by their morphological features and density within the weak atmospheric turbulence. Figure 9(*a*) juxtaposes the normalized acceleration p.d.f.s of different snow types against the acceleration of fluid parcels in homogeneous isotropic turbulence, based on simulations by Bec *et al.* (2006). It is generally anticipated that, due to inertia, particles in turbulence will not accelerate as intensely as the surrounding fluid because they cannot keep pace with the rapid fluctuations of the turbulent flow. Nevertheless, the shape of the particles is also

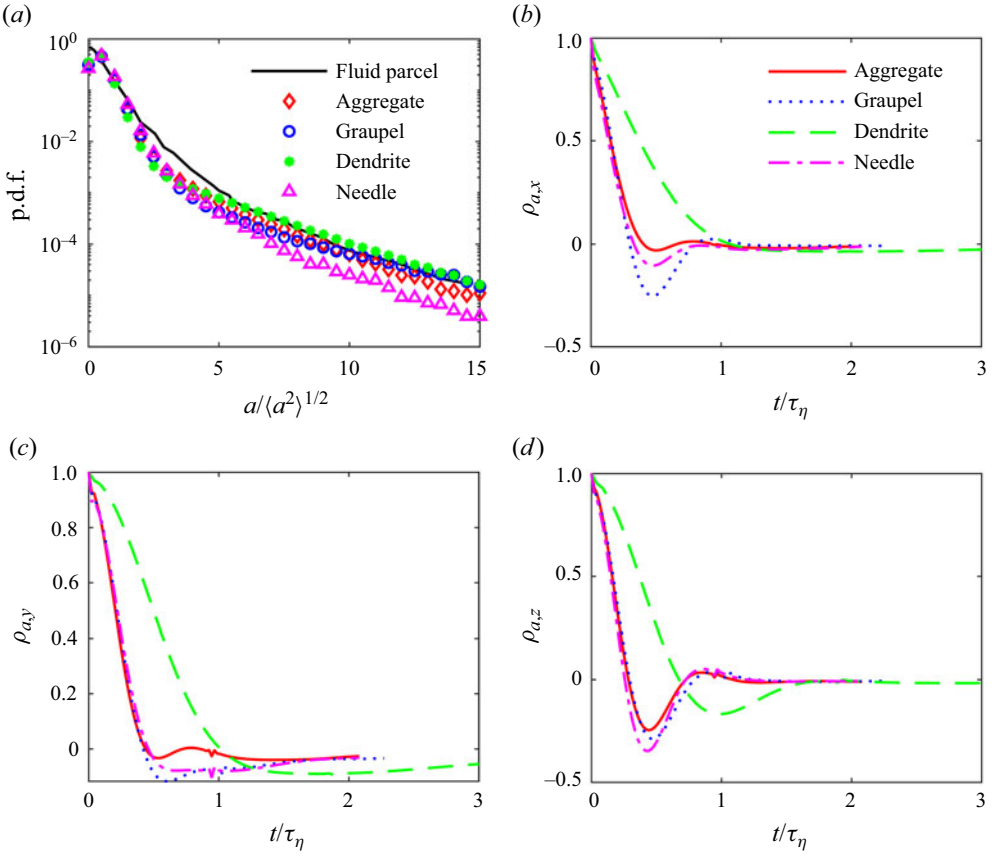

Figure 9. (*a*) Probability density functions of acceleration across four snow particle types – aggregates (red diamonds), graupel (blue circles), dendrites (green stars) and needles (magenta triangles) – set against the benchmark fluid parcel acceleration from homogeneous isotropic turbulence, as reported by Bec *et al.* (2006). (*b–d*) Acceleration autocorrelation functions, (*b*) $\rho_{a,x}$, (*c*) $\rho_{a,y}$ and (*d*) $\rho_{a,z}$, averaged from these snow particle trajectories, with each type depicted by the following colour and line style: aggregates (red solid line), graupel (blue dotted line), dendrites (green dashed line) and needles (magenta dash-dotted line). The x axis, temporal difference, is normalized by the Kolmogorov time scale.

a critical factor in their acceleration dynamics. Dendrites, for instance, are more prone to high acceleration events, likely a consequence of their considerable size, expansive frontal area and the nonlinear nature of the drag forces they experience. Aggregates and graupels display a decrease in the probability of high accelerations, attributable to their less intricate shapes. Needles, characterized by their slender profile, exhibit a diminished probability of encountering higher acceleration events, which may be due to their streamlined shape that naturally aligns with the flow and vortex structures within, along with their smaller size and frontal area (Voth & Soldati 2017). The p.d.f. tails of these non-spherical particles also appear to correlate with their shape factors, with needles being prolate ($\beta > 1$), dendrites oblate ($\beta < 1$) and aggregates displaying a spectrum in between these extremes. This observation contrasts with the recent findings reported by Singh, Pardyjak & Garrett (2023), which provides a universal scaling for snow particle acceleration. Additional experimentation under various turbulence conditions is needed to further investigate this discrepancy.

Snow type	$\overline{a_{f,horz}}$ (m s^{-2})	$\overline{a_{f,z}}$ (m s^{-2})	$\overline{f_{horz}}$ (Hz)	$\bar{f}_z$ (Hz)	$St = \overline{f_{horz}} \times \overline{D_p}/\overline{W_s}$ (–)	$4\tau_{0,x}$ (s)	$4\tau_{0,y}$ (s)	$4\tau_{0,z}$ (s)	τ_η (s)
Aggregate	0.27	0.60	2.6	3.8	2×10^{-3}	0.38	0.42	0.27	0.24
Graupel	0.19	0.45	5.6	6.6	4×10^{-3}	0.26	0.36	0.26	0.22
Dendrite	0.30	0.47	2.0	3.3	2×10^{-3}	0.51	0.48	0.32	0.12
Needle	0.22	0.55	2.5	4.1	1×10^{-3}	0.32	0.44	0.24	0.24

Table 4. Comparative summary of horizontal and vertical acceleration variations in snow particle trajectories, presenting the average magnitude ($\overline{a_{f,horz}}$, $\overline{a_{f,z}}$) and frequency ($\overline{f_{horz}}$, $\bar{f}_z$), alongside the zero-crossing times ($\tau_{0,x}$, $\tau_{0,y}$ and $\tau_{0,z}$) of the acceleration autocorrelation functions and the Kolmogorov time scale (τ_η), for different snow particle types.

In figure 9(*b–d*) the acceleration autocorrelation functions of the Lagrangian acceleration components reveal distinct inertial responses for the four types of snow particles. These functions are derived from the snow particles' settling trajectories, using the formula $\rho_a(n\Delta t) = \langle a(t_0)a(t_0 + n\Delta t)\rangle/\langle a^2\rangle$, where n is the number of time steps and $\Delta t = 1/200$ s is the time step. Dendrites display the highest inertia, indicating a more pronounced resistance to changes in the fluid motion, followed by aggregates, needles and graupels (small differences among the three for all components). The particle inertia is attributable to the larger sizes of dendrites and aggregates, their non-spherical shapes and their greater density in the case of dendrites and needles. The zero-crossing points (τ_0) on the autocorrelation curves also provide temporal insights into the acceleration fluctuations and, consequently, the frequency of the meandering motions of the snow particles, as listed in table 4. It scales with one-fourth the period of the meandering motion. In table 4 we present a comparison of four times the zero-crossing time ($4\tau_0$) of the acceleration autocorrelation function for the three acceleration components across various snow particle types. Generally, dendrites exhibit the largest zero-crossing time scales in their acceleration autocorrelation functions, suggesting a low-frequency meandering motion. Conversely, graupels demonstrate the smallest zero-crossing time scales, suggesting the fastest meandering frequency, corroborating the qualitative observations from figure 7. The acceleration autocorrelation functions for needles and aggregates reach their initial zero at intermediary times, with aggregates showing slightly larger time scales. The trends in these autocorrelation functions further emphasize the influence of particle morphology on settling behaviour, with the aspect ratios of non-spherical particles mirroring the trends in the zero-crossing time scales.

Following up the autocorrelation functions of acceleration above, we provide a more direct measurement of the meandering motion of snow particles by examining the Lagrangian variations in position, velocity and acceleration along their settling trajectories, as shown in figure 8. The horizontal acceleration component, displaying the most pronounced variation, serves as a key indicator of meandering behaviours, as illustrated in figure 10(*a*,*b*), which depict the p.d.f.s of acceleration fluctuation frequency and magnitude for different snow particle types. This analytical approach aligns with the qualitative findings from figure 7 and supports the acceleration statistics presented in figure 9. The measured average frequencies and corresponding magnitudes are summarized in table 4. These frequencies can be non-dimensionalized into Strouhal numbers, $St = \overline{f_{horz}} \times \overline{D_p}/\overline{W_s}$, as proposed by Willmarth *et al.* (1964), and summarized in table 4. Although the near-spherical shape of graupels is not expected to induce meandering motion, our measurements surprisingly reveal a weak meandering or helical

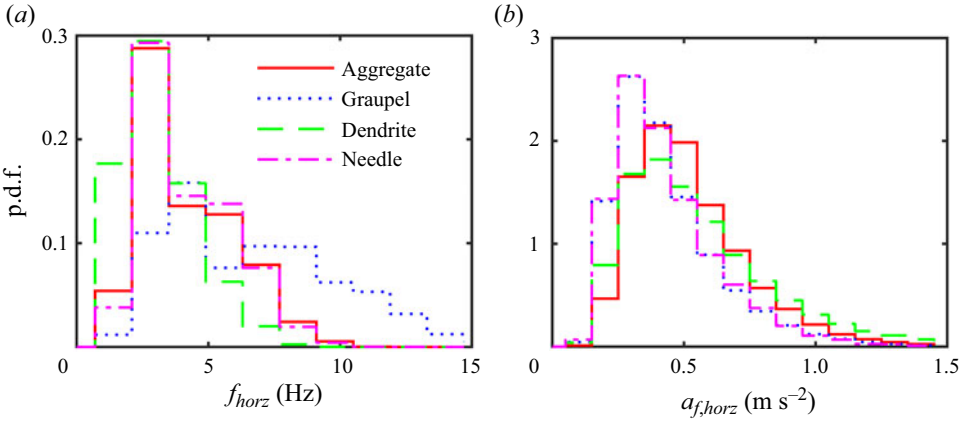

Figure 10. (*a*) Probability density functions of the frequency of horizontal acceleration fluctuations (f_{horz}) and (*b*) p.d.f.s of the magnitude of these fluctuations ($a_{f,horz}$) across four snow particle types. Aggregates are represented by red solid lines, graupels by blue dotted lines, dendrites by green dashed lines and needles by magenta dash-dotted lines.

motion, as evidenced by variations in velocity and acceleration. The observed average frequency of this motion closely matches the Kolmogorov scale frequency $1/\tau_\eta = 4.6$ Hz. This correspondence suggests that, despite the dominance of morphological effects in dictating particle behaviour, especially for non-spherical particles, graupels still move around and weakly interact with the Kolmogorov eddies within the flow, considering their sizes close to those of the Kolmogorov eddies. In contrast, the meandering frequencies for non-spherical particles are lower than both the frequency corresponding to the Kolmogorov scale and the vortex shedding frequency in the wake of anisotropic particles identified in various studies (Willmarth *et al.* 1964; Jayaweera & Mason 1965; Auguste *et al.* 2013; Toloui *et al.* 2014; Tinklenberg *et al.* 2023). Specifically for dendrites, we estimate the dimensionless moment of inertia to be $\sim O(0.1-1)$, resulting in the Strouhal number $\sim O(0.01)$ based on Willmarth *et al.* (1964), larger than that of the dendrites from our measurement. This discrepancy may be attributable to the delayed inertial response of non-spherical particles to the fluid flow and vortex shedding, as well as to the permeability of the dendrites. Moreover, the measured Strouhal numbers for these particles are consistent with Kajikawa's laboratory measurements (Kajikawa 1976, 1982, 1989, 1992; Kajikawa & Okuhara 1997), situating our findings within the observed range for the meandering motions of non-spherical snow particles. The vertical acceleration component displays fluctuations that could stem from orientation changes (resulting in drag force variation) in anisotropic particles due to horizontal meandering. The a_z fluctuation magnitudes are more pronounced since the horizontal component combines the x and y components, which are typically out of phase. Furthermore, the vertical acceleration fluctuation frequency is nearly twice the horizontal one because the inferred changes in particle orientation, caused by horizontal meandering, e.g. a perfectly edge-on configuration, have a 180° periodicity for disk- and needle-like shapes. This interpretation is consistent with the minimal differences observed for the near-symmetric graupel, and the trend is also consistent with the shorter zero-crossing times ($\tau_{0,z}$) observed in our data.

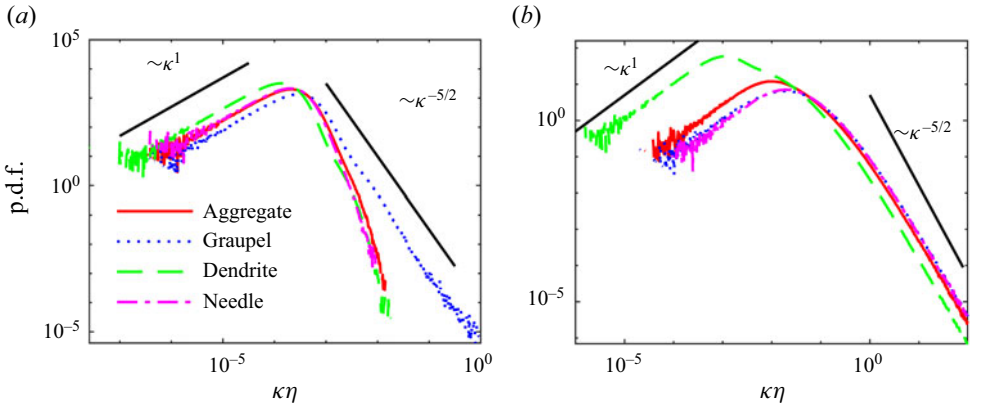

Figure 11. (*a*) Probability density functions of the normalized trajectory curvature ($\kappa\eta$, normalized by the Kolmogorov scale) for four different snow particle types using original path data. (*b*) Probability density functions of normalized curvature after adjusting for the mean streamwise flow and settling velocities. Each snow type is depicted by a distinctive line style and colour: aggregates with red solid lines, graupel with blue dotted lines, dendrites with green dashed lines and needles with magenta dash-dotted lines.

3.2.4. *Trajectory geometry*

The variance in meandering frequency and magnitude across different types of snow particles results in distinctive trajectories. To quantify their geometrical differences, we employ curvature calculations both with and without the impact of the mean streamwise and settling velocities. Figure 11 illustrates the p.d.f.s of these normalized trajectory curvatures ($\kappa\eta$, where η is the Kolmogorov scale). For the original trajectories, curvature is calculated using the formula $\kappa = \|\boldsymbol{u}\times\boldsymbol{a}\|/\|\boldsymbol{u}\|^3$ (figure 11*a*), where $\times$ indicates the cross-product between the velocity ($\boldsymbol{u}$) and acceleration ($\boldsymbol{a}$) vectors. Additionally, to minimize the influence of varying flow and settling velocities across datasets, we adjust the velocity vector to $\boldsymbol{u}' = (u_x - \overline{u_x}, u_y, u_z - \overline{u_z})$), and recompute curvature (figure 11*b*). Previous research by Braun, De Lillo & Eckhardt (2006), Xu, Ouellette & Bodenschatz (2007) and Scagliarini (2011) has explored the geometry of fluid trajectories in turbulence, uncovering characteristic scaling within the curvature p.d.f.s. Their findings suggest a universal scaling for both tails of the p.d.f.s: low curvature events scale with κ^1, while high-curvature events follow a $\kappa^{-5/2}$ scaling. Xu *et al.* (2007) propose that these tail scaling laws result from Gaussian velocity statistics rather than turbulence gradients, contending that high-curvature events correlate with periods of low velocity rather than high acceleration from interactions with thin vortex tubes as one might expect. Moreover, curvature can also be expressed as $\kappa = \|a_n\|/\|\boldsymbol{u}\|^2$, so the tail of the curvature p.d.f., $P_{\kappa\to\infty}$, as $\kappa\to\infty$, scales similarly to the tail of the p.d.f. of $\boldsymbol{u}^{-2} = 1/(u_x^2+u_y^2+u_z^2)$, $P_{\boldsymbol{u}^{-2}\to\infty}$, as $\boldsymbol{u}^{-2}\to\infty$. Assuming velocity components are independent and follow Gaussian statistics, $P_{\boldsymbol{u}^{-2}\to\infty}$ conforms to a chi-square distribution with three degrees of freedom, leading to the derived scaling of $P_{\kappa\to\infty}\sim\kappa^{-5/2}$. Bhatnagar *et al.* (2016) extended this theoretical framework to heavy inertial particles and verified through simulations that the same scaling applies to the p.d.f.s of these particles' trajectories. These theoretical insights can be integrated into our analysis of the geometry of snow particle trajectories, providing a better understanding of the intricate settling dynamics and trajectory geometry under the influential role of particle morphology.

Figure 11(*a*,*b*) reveals that for most snow particle types, the tails of the curvature p.d.f.s exhibit similar scaling trends as reported in previous research (Braun *et al.* 2006; Xu *et al.*

2007; Scagliarini 2011; Bhatnagar *et al.* 2016). Nonetheless, when considering the mean streamwise and settling motions, the p.d.f.s of curvature for non-spherical particles exhibit a notably different scaling, approximately following a κ^{-4} trend as shown in figure 11(*a*). This deviation may arise from the rotation and meandering motion due to the morphology of non-spherical snow particles, which modulates the Lagrangian velocities along the trajectories. Notably, when the mean settling and streamwise velocities are removed from consideration, the tails of the curvature p.d.f.s for different snow types tend to align on the higher curvature end. This pattern indicates that particle morphology predominantly influences the mean values of the settling and streamwise velocities, rather than their fluctuations. Moreover, the peaks of the p.d.f.s are around 10^{-2} and 10^{-3}, similar to those in the previous studies. However, as proposed by Xu *et al.* (2007), for fluid tracers, the peak of the p.d.f. scale with $(\eta Re_\lambda)^{-1}$, which for the snow particle trajectories, would be $\sim O(1)$. The smaller curvature for the snow particle trajectories might be attributed to the particle inertia (Maxey 1987). Further analysis shows that, despite the pronounced meandering behaviour of dendrites, they exhibit the smallest mean curvature, with aggregates, needles and graupels following in ascending order. This trend can be explained by the fact that both the frequency and magnitude of the meandering motion contribute to the overall trajectory curvature. Dendrite trajectories, while displaying significant fluctuations in spanwise meandering motion, have a lower frequency, which culminates in a reduced mean curvature. The observed differences in the curvature p.d.f.s for graupels and other non-spherical snow types can be elucidated by drawing upon our earlier analysis in § 3.2.3. For graupels, the curvature p.d.f. in figure 11(*a*) scales like that of fluid trajectories, indicating that the weak meandering behaviour of graupels may stem from interactions with turbulent eddies. In contrast, for non-spherical particles, it is likely due to the combined influence of wake vortex instabilities, as discussed in § 3.2.3, and weak atmospheric turbulence, as the scaling later converged in figure 11(*b*).

Figure 12 then delves into the relationship between normalized spanwise velocity ($|u_y|/\overline{W_s}$) and normalized trajectory curvature ($\kappa\eta$) for snow particles, taking into account the theoretical finding by Xu *et al.* (2007) that high-curvature events tend to coincide with low velocities. While snow particles settling in the atmosphere generally have non-zero streamwise and settling velocities, high-curvature events are often tied to moments when the spanwise velocity is minimal and changing sign. This trend is evident in figures 7 and 8(*a*), where the spanwise velocity approaches zero and reverses direction at the peaks of the meandering motion, leading to increased curvature at these turning points. In figure 12, joint p.d.f.s map the spanwise velocity magnitude and the local trajectory curvature, after subtracting the mean streamwise and settling velocities, for each snow particle type. A pronounced negative correlation between spanwise velocity and trajectory curvature is observed, particularly for dendrites (figure 12*c*), which exhibit the most substantial correlation coefficient ($\sigma_{xy} = -0.80$). Aggregates display a similar negative correlation, but with a slightly lower coefficient ($\sigma_{xy} = -0.77$) and a reduced magnitude of spanwise velocity. Needles, despite having the lowest spanwise velocity magnitude potentially due to their smaller frontal area and high density, maintain a strong correlation with curvature, indicated by a correlation coefficient of $\sigma_{xy} = -0.76$. Graupels, on the other hand, show the weakest correlation among all particle types, with the lowest coefficient ($\sigma_{xy} = -0.71$). This analysis highlights the profound effect of snow particle morphology on meandering motion for non-spherical particles, which associates the near-zero spanwise velocity in the meandering extremes with the high curvature in their trajectories. Unlike graupels, whose weaker meandering motion is influenced more by interactions with turbulence eddies, non-spherical particles do not exhibit the expected correlation between high curvature and

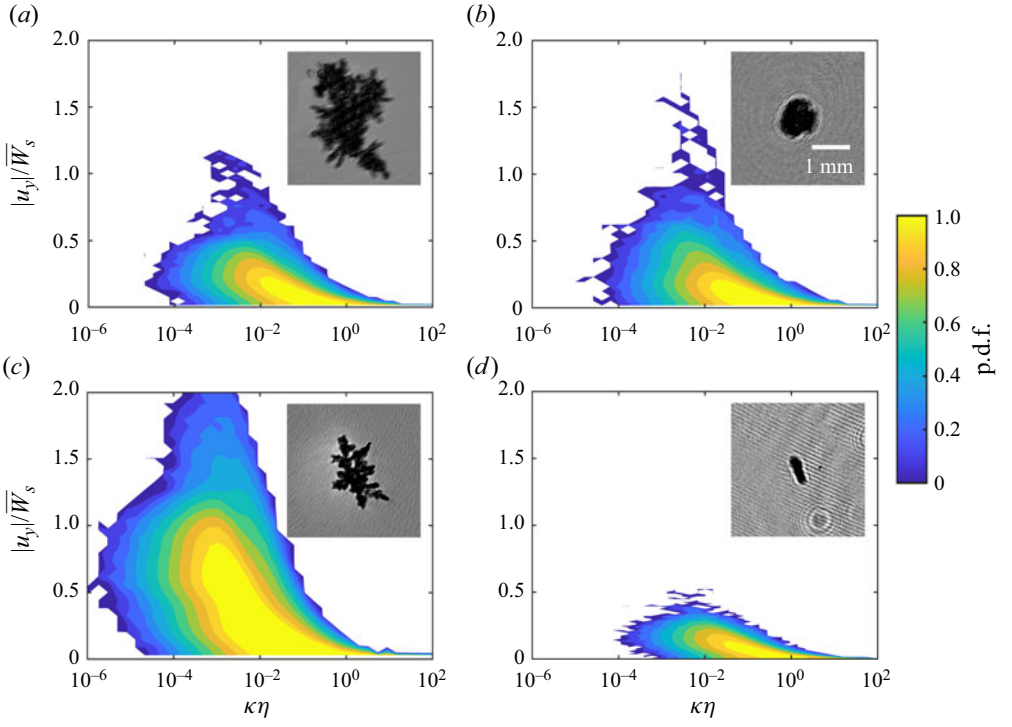

Figure 12. Joint p.d.f.s depicting the interdependence of normalized spanwise velocity magnitude ($|u_y|/\overline{W_s}$) and normalized trajectory curvature ($\kappa\eta$) for four types of snow particles: (*a*) aggregates, (*b*) graupel, (*c*) dendrites and (*d*) needles. The colour gradient indicates the probability of data occurrence, with warmer colours representing higher concentrations. Insets provide sample holograms of typical particles from each type.

high acceleration, suggesting that their complex morphology dominates this meandering motion and corresponding high-curvature events.

3.3. *Interconnection between trajectory geometry and settling velocity*

Our comprehensive analysis elucidates the distinctive settling behaviours of snow particles with various morphologies, addressing the questions raised at the beginning of our results section. Concerning the influence of morphology on snow aerodynamic properties, we observe that the response times for all snow particles are broadly similar, averaging around 0.1 s, of the same order of the intercept in the acceleration autocorrelation function. However, needles exhibit a marginally increased response time attributed to their higher density, particularly when compared with the density of the surrounding air. This higher density contributes to the needles' higher average terminal velocity in still air. Furthermore, the empirical models by Böhm (1989) well predict the drag coefficients for aggregates, graupels and needles, while dendrites emerge as anomalies, exhibiting drag coefficients exceeding model predictions, likely due to their large frontal area and oblate, disk-like, geometry. Notably, although dendrites and needles have similar aspect ratios, as measured by the snow particle analyser, the dendrites are disk-like, oblate spheroids, while the needles are columnar, prolate spheroids.

The different aerodynamic properties and morphologies of these snow particles have strong effects on their settling kinematics. Specifically, dendrites display unique behaviour

compared with other types. Their nonlinear drag and substantial frontal area result in the most prominent acceleration fluctuation magnitude, occurring at relatively low frequencies. While the acceleration p.d.f. for dendrites closely resembles that of a fluid parcel in turbulence, the acceleration autocorrelation function indicates a slow response to the rapid fluctuation of the flow velocity. Conversely, needles exhibit minimal acceleration fluctuation magnitude, suggesting relatively large inertia and a tendency to avoid intense cross-flow drag and convoluted trajectories. Yet, the acceleration autocorrelation function indicates a moderate rate of change in the direction of acceleration. Such different behaviours from that of dendrites are possibly due to their streamlined shape aligning with fluid flow structures, as for fibres in turbulence. Overall, acceleration statistics appear to correlate with the shape factors of these particles considered as spheroids, with dendrites and needles representing the spectrum's extremes and aggregates positioned in between.

Finally, to answer the third question, it becomes apparent, from our analysis above, that the combination of turbulence and non-spherical particle morphologies can modulate the particle settling velocities even under weak atmospheric turbulence. For the cases investigated here, we hypothesize that dendrites exhibit an enhanced settling velocity (figure 5*c*) that is due to an underestimation of the drag coefficient in the model by Böhm (1989); graupels settling velocity is well predicted even though spherical particles smaller than the Kolmogorov scale and close to critical Stokes conditions were expected to exhibit settling velocity enhancement. The significant cross-flow velocities (considering the large settling parameter Sv_L) experienced by graupels may suggest that preferential sweeping was not the only mechanism in play during settling. Aggregates drag coefficient is well captured in the still-air model, implying that the observed enhanced settling is likely due to combined effects of anisotropic particle orientation and the weak atmospheric turbulence. The observed conditions are marked by $St_\eta Sv_L \sim 1$ for which settling enhancement has been predicted and observed (Petersen *et al.* 2019; Brandt & Coletti 2022). Disentangling turbulence and morphology effects is challenging because turbulence-induced disturbances alter the preferential orientation (i.e. particles with their largest projected area facing the settling direction) of stably falling particles. The meandering motions of the non-spherical particles, whether fluttering or tumbling, likely affect their orientation, reducing their average projected area compared with a steady settling and thus enhancing settling velocity. However, direct measurement of particle orientation during settling is technically challenging and beyond our current capability.

Thus, we investigate the interconnection between the meandering motion and the vertical acceleration along the trajectories of snow particles. Recognizing that these fluctuations might not be perfectly synchronized (owing to the particles' inertial response and the variability in drag force related to changes in projected area and settling velocity), we have considered a slight phase shift between the varying spanwise location $y(t)$ and vertical acceleration $a_z(t+\tau)$ along the trajectories. This adjustment aims to align the locations of maximum meandering with the smallest projected area, which typically corresponds to greater downward acceleration. To maintain the integrity of the correlation, we limit the phase shift to 0.15 times a quarter of the meandering period to avoid creating an inverse relationship between vertical acceleration and meandering motion. Note that this time lag (τ) is of the order of $0.1\tau_p$, and close to the estimated Strouhal number for the disk-like particles. Thus, during a fraction of the anisotropic particle rotation and the corresponding translational response time, the particle is experiencing a reduction in drag area, leading to its acceleration downward. Figure 13(*a*,*b*) demonstrates that, following this phase shift, the greatest downward accelerations predominantly occur at the furthest extent of the spanwise meandering motion ($y'_{a,max} \sim 1$). Conversely, the least downward

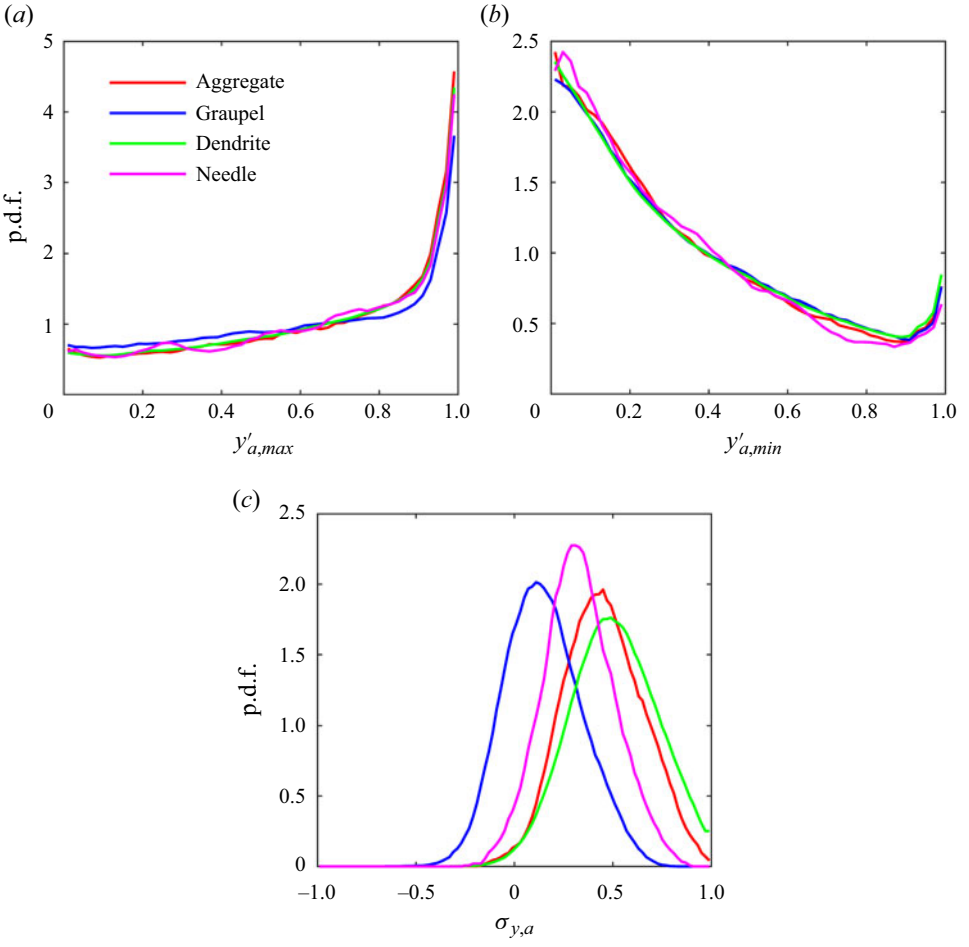

Figure 13. (*a*,*b*) Probability density functions of the spanwise snow particle positions, normalized by its maximum excursion for each trajectory, conditioned on high ($y'_{a,max}$) and low ($y'_{a,min}$) values of the vertical accelerations, and categorized by four snow particle types: aggregates (red), graupels (blue), dendrites (green) and needles (magenta). (*c*) Probability density functions of the correlation coefficients ($\sigma_{y,a}$) between the normalized spanwise position and the downward (positive) acceleration for these particles throughout their meandering path. Note that the spanwise particle locations $y(t)$ and corresponding vertical accelerations $a_z(t)$ are slightly temporally shifted to account for the response of the particle acceleration to change in orientation.

acceleration – or even upward acceleration – tends to happen near the central position ($y'_{a,min} \sim 0$), where anisotropic snow particles are likely to have their maximum projected area facing downwards. Subsequently, we calculate the correlation coefficient between vertical acceleration and spanwise position during the snow particles' meandering motion. The results reveal substantial positive correlation coefficients for dendrites ($\overline{\sigma_{y,a}} = 0.58$) and aggregates ($\overline{\sigma_{y,a}} = 0.45$), which is consistent with their observed enhanced settling velocities. Needles display a moderate correlation coefficient ($\overline{\sigma_{y,a}} = 0.33$), reflective of their anisotropic shape. Graupels, however, exhibit a low average correlation coefficient of $\overline{\sigma_{y,a}} = 0.15$, as changes in particle orientation are not expected to significantly affect the drag force.

4. Conclusions and discussion

In this study we conduct a comprehensive field investigation into the 3-D settling dynamics of snow particles under weak atmospheric turbulence. This investigation was enabled by a field 3-D PTV system (Bristow *et al.* 2023), recording over a million settling trajectories for four distinct types of snow particles (i.e. aggregates, graupels, dendrites, needles) and by simultaneous characterization of their aerodynamic properties using a holographic snow particle analyser (Li *et al.* 2023). We have examined the snow particle aerodynamic properties, including terminal velocity in air, settling velocity, drag coefficient, settling kinematics including acceleration statistics and trajectory geometry, and the interconnection between the observed meandering path and settling velocity of the snow particles. The comparison between the estimated terminal velocity (Böhm 1989) and the measured settling velocity demonstrate that non-spherical particles, especially aggregates and dendrites, exhibit large differences between measurements and model predictions potentially due to dynamic orientation changes along their meandering paths, which is not observed in graupels. Specifically, the settling enhancement observed in aggregates is likely a synergistic result between morphology-induced oscillations due to vortex shedding and the ambient flow that promotes wake instabilities and the onset of meandering motions. Even though dendrites are characterized by a higher drag coefficient, as compared with other snow types, corroborating the laboratory findings of Tagliavini *et al.* (2021*a*), their settling velocity under weak atmospheric turbulence is higher than model predictions assuming a nominal flat-falling drag area (Böhm 1989). These apparently contradicting results emphasize the need to quantify particle settling dynamics along their complex trajectories in the field. A detailed Lagrangian analysis reveals that dendrites and aggregates undergo pronounced meandering motions in the horizontal plane perpendicular to the direction of gravity at relatively lower frequencies, likely governed by their inertia to tumbling and rotation but enabled by ambient turbulence. Needles, however, exhibit weaker meandering amplitudes due to their smaller frontal area. Graupels, despite their near-spherical form, undergo oscillatory motions along their settling paths, characterized by higher frequencies comparable to the Kolmogorov scale and smaller amplitudes. This behaviour suggests a limited interaction with small-scale turbulence structures under the conditions investigated, a notion corroborated by the agreement between model-predicted terminal velocities and measured settling velocities. These distinct settling motions and styles are also reflected in the curvature statistics, differentiating non-spherical particles from graupels. More specifically, the analysis of vertical acceleration during meandering paths reveals that periodic changes in the orientation of non-spherical particles, especially dendrites and aggregates, contribute to their enhanced settling velocity. These findings highlight the dominant impact of the morphology of snow particles on their settling dynamics under weak atmospheric turbulence.

In light of these observations and insights, our current study provides a unique dataset that captures realistic snow morphologies and their corresponding settling trajectories. These measurements contribute to the modelling and simulation of snow settling velocity and subsequent snow accumulation rate on the ground. Despite the dominant morphology effect, interactions between the snow particles and the weak atmospheric turbulence are still manifested in some aspects of their settling dynamics. Although the non-spherical particles are likely to rotate or tumble when settling in quiescent flow, disturbances by the ambient flow promote these unsteady motions. Besides, the meandering motion of graupels exhibits frequencies closest to that of the Kolmogorov scale, hinting at a weak interaction with the ambient turbulence. The weak turbulence effect is also

manifested in the curvature statistics of the particle trajectories. We observe distinct scaling laws for the high-curvature tails of the p.d.f.s, which mark differences between spherical particles, consistent with Xu *et al.* (2007) for fluid trajectories in turbulence and Bhatnagar *et al.* (2016) for inertial particles, and non-spherical particles, hinting at morphological influences on their settling kinematics. To compensate for variations in streamwise flow velocity and settling velocity across different datasets and morphologies, we have corrected the curvature formulation. The resulting high-curvature tails of the p.d.f.s converge to a universal scaling associated with low spanwise velocity, reinforcing the concept that high-curvature events are associated with the meandering motions of non-spherical particles. This association is further emphasized by the observed inverse correlation between the trajectory curvature and spanwise velocity. Our detailed characterization of the snow particle morphology, density and settling velocity may lead to an improved prediction of ground snow accumulation, benefiting several related applications in snow hazard warning, climate modelling and traffic regulation during/after snowfall.

Despite our major findings that substantiate the hypothesis of strong morphological effects on dictating snow particle settling dynamics under conditions of weak atmospheric turbulence, several challenges persist. First, quantifying the exact enhancement or hindrance of settling velocities due to weak atmospheric turbulence remains a challenging task. A better model that elaborates on the interplay between particle morphology and turbulence will be necessary. Second, current predictive models, including those by Böhm (1989), fall short in estimating the aerodynamic properties, especially the drag coefficient, for dendrites. There is a clear need for refined models that can more accurately represent these unique and complex snow particle types. Third, while we aimed to correlate the meandering motion and orientation changes to enhanced settling in non-spherical particles, the spatial resolution of our 3-D PTV system is insufficient for capturing the orientation dynamics of particles throughout their settling. Some of the smaller particles captured by the snow particle analyser might also exhibit too weak a signal to be detected by the 3-D PTV system. Advancements in measurement systems could enable simultaneous assessments of particle orientation and settling trajectory and higher resolution for capturing smaller snow particles. Systems such as a high-magnification, high-resolution 3-D PTV (Marcus *et al.* 2014; Leinonen, Grazioli & Alexis 2021) or a DIH set-up with an expanded field of view (Wu *et al.* 2015; Li *et al.* 2023) and higher sampling rate, hold promise for the desired measurements. Finally, the variability of field conditions presents an additional layer of complexity. Snow particle types and concentrations, as well as average wind speed and direction, are subject to change over each measurement period, which typically spans 3–5 h. The relatively slow streamwise wind adds to the difficulty of accurately estimating turbulence quantities. Looking ahead, we aim to extend our investigations to scenarios involving moderate to intense turbulence. By contrasting the settling behaviours across a spectrum of turbulence intensities, particularly for different snow particle morphologies, we anticipate a more thorough understanding of how turbulence and snow particle morphology collectively influence the settling dynamics of snow particles. This future research will enable us to improve our predictive capabilities of snow settling velocity and, in the long term, of the spatial distribution and intensity of snow accumulation on the ground during snowfalls.

Acknowledgements. The authors thank Dr N. Bristow, P. Hartford and S. Purohit for their assistance in the experiments.

Funding. This work was supported by the National Science Foundation (Program Manager, Nicholas Anderson) under grant NSF-AGS-1822192 before May 2023.

Declaration of interests. The authors report no conflict of interest.

Data availability statement. The data that support the findings of this study are openly available in Data Repository for the University of Minnesota (DRUM) at https://doi.org/10.13020/emmw-5f12.

Author ORCIDs.
Jiaqi Li https://orcid.org/0000-0002-1201-7489;
Michele Guala https://orcid.org/0000-0002-9788-8119;
Jiarong Hong https://orcid.org/0000-0001-7860-2181.

Appendix A

We employ a Gaussian kernel as a low-pass filter to reduce uncertainties in determining the 3-D positions of snow particles and to prevent these errors from affecting Lagrangian statistics. Large errors typically occur at the trajectory ends after filtering; therefore, these segments are excluded from the statistical analysis. The selection of the kernel size is critical. A kernel that is too short fails to sufficiently reduce position uncertainty, while a kernel that is too long may suppress genuine strong acceleration events. We optimize the kernel size by analysing the change in acceleration variance, defined as $a_0 = \langle a'^2 \rangle \nu^{1/2}/\varepsilon^{3/2}$, across varying kernel sizes. As shown in figure 14, this approach enables the identification of the optimal kernel size. We determined that a minimal kernel size of 45 frames best maintains the exponential dependency of acceleration variance on kernel size. Notably, this selected kernel size, τ_g, is comparable to the Kolmogorov length scale, τ_η, corroborating findings from previous studies (Voth *et al.* 2002; Gerashchenko *et al.* 2008; Nemes *et al.* 2017). The estimated uncertainty in the acceleration measurements reflects the uncertainty in the filter size, which ranges between 43 and 47 frames. This results in the root-mean-square error in acceleration estimation, a_{rms}, ranging between 0.32 and 0.38 m s^{-2} for different snow particle types, which lead to the uncertainty of velocity measurement to be around 0.002 m s^{-1} as $\delta_v = \delta_a \, \mathrm{d}t$.

Appendix B

To more accurately model the drag coefficient of snow particles, significant efforts have been made by researchers (Böhm 1989; Heymsfield & Westbrook 2010; McCorquodale & Westbrook 2021). The illustrations in figure 15 summarize and clarify the calculations used in this study. The drag coefficient of snow particles can be defined using either the projected area, $C_{De} = f(A_e)$, or the circumscribed area, $C_D = f(A)$. According to Böhm (1989), the two drag coefficients are correlated by the area ratio, $C_{De}/C_D = (A/A_e)^{3/4}$, where C_D is defined by (2.2). Thus, to compare the model ($C_{De} = (A/A_e)^{3/4} C_0(1 + \delta_0/Re_p^{1/2})^2$) with the measured drag coefficient ($C_{De,mean}$), as discussed in § 3.1, it is necessary to calculate the maximum projected area, $A_{e,max}$. Given that our snow particle analyser only measures the general projected area (A_e) and the circumscribed area (A) at an unknown orientation, we assume that the ratio A/A_e remains constant regardless of orientation. Consequently, the maximum projected area can be estimated as $A_{e,max} = A_{max}(A_e/A)$. In this equation, the maximum circumscribed area is calculated as $A_{max} = \pi D_{maj}^2/4$ for plates and dendrites and as $A_{max} = \pi D_{maj} D_{min}/4$ for other snow particle types, where D_{maj} and D_{min} are measured by the snow particle analyser.

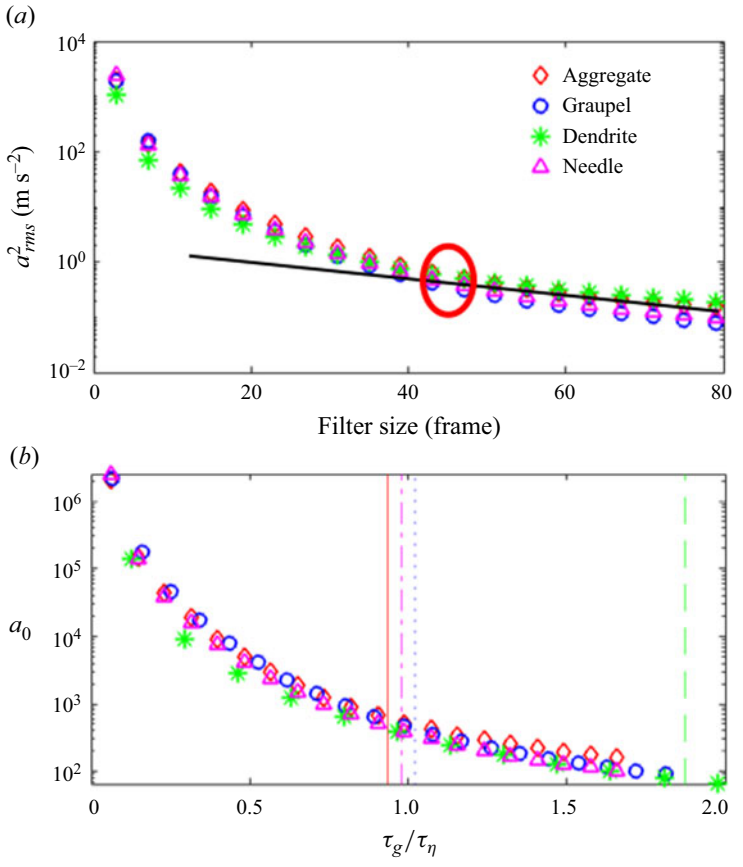

Figure 14. (*a*) The variation of the mean square of the acceleration fluctuation with the increasing Gaussian filter length. The black line represents the exponential fit and the red circle identifies the optimal filter length. The red diamonds represent aggregates, blue circles for graupels, green stars for dendrites and magenta triangles for needles. (*b*) The normalized acceleration variance ($a_0 = \langle a'^2 \rangle v^{1/2}/\varepsilon^{3/2}$) as a function of the filter length (τ_g) normalized by the Kolmogorov time scale (τ_η). The vertical lines indicate the selected filter length for different snow particle types.

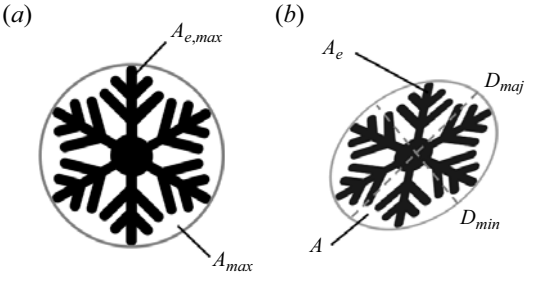

Figure 15. The illustration on (*a*) defines the maximum projected area ($A_{e,max}$) and the maximum circumscribed area (A_{max}) of a dendrite snow particle when oriented downward. The illustration on (*b*) defines the general projected area (A_e), the circumscribed area (A), the major axis length (D_{maj}) and the minor axis length (D_{min}) of a dendrite snow particle in any orientation.

References

Aliseda, A., Cartellier, A., Hainaux, F. & Lasheras, J.C. 2002 Effect of preferential concentration on the settling velocity of heavy particles in homogeneous isotropic turbulence. *J. Fluid Mech.* **468**, 77–105.

Auguste, F., Magnaudet, J. & Fabre, D. 2013 Falling styles of disks. *J. Fluid Mech.* **719**, 388–405.

Bec, J., Biferale, L., Boffetta, G., Celani, A., Cencini, M., Lanotte, A., Musacchio, S. & Toschi, F. 2006 Acceleration statistics of heavy particles in turbulence. *J. Fluid Mech.* **550**, 349–358.

Bec, J., Homann, H. & Ray, S.S. 2014 Gravity-driven enhancement of heavy particle clustering in turbulent flow. *Phys. Rev. Lett.* **112** (18), 184501.

Bhatnagar, A., Gupta, A., Mitra, D., Perlekar, P., Wilkinson, M. & Pandit, R. 2016 Deviation-angle and trajectory statistics for inertial particles in turbulence. *Phys. Rev.* E **94** (6), 063112.

Böhm, H.P. 1989 A general equation for the terminal fall speed of solid hydrometeors. *J. Atmos. Sci.* **46** (15), 2419–2427.

Brandt, L. & Coletti, F. 2022 Particle-laden turbulence: progress and perspectives. *Annu. Rev. Fluid Mech.* **54**, 159–189.

Braun, W., De Lillo, F. & Eckhardt, B. 2006 Geometry of particle paths in turbulent flows. *J. Turbul.* **7**, N62.

Bristow, N., Li, J., Hartford, P., Guala, M. & Hong, J. 2023 Imaging-based 3D particle tracking system for field characterization of particle dynamics in atmospheric flows. *Exp. Fluids* **64** (4), 78.

Cho, H.R., Iribarne, J.V. & Richards, W.G. 1981 On the orientation of ice crystals in a cumulonimbus cloud. *J. Atmos. Sci.* **38** (5), 1111–1114.

Clark, M.P., Hendrikx, J., Slater, A.G., Kavetski, D., Anderson, B., Cullen, N.J., Kerr, T., Örn Hreinsson, E. & Woods, R.A. 2011 Representing spatial variability of snow water equivalent in hydrologic and land-surface models: a review. *Water Resour. Res.* **47** (7), W07539.

Dasari, T., Wu, Y., Liu, Y. & Hong, J. 2019 Near-wake behaviour of a utility-scale wind turbine. *J. Fluid Mech.* **859**, 204–246.

Esteban, L.B., Shrimpton, J.S. & Ganapathisubramani, B. 2020 Disks settling in turbulence. *J. Fluid Mech.* **883**, A58.

Falkinhoff, F., Obligado, M., Bourgoin, M. & Mininni, P.D. 2020 Preferential concentration of free-falling heavy particles in turbulence. *Phys. Rev. Lett.* **125** (6), 064504.

Field, P.R., Heymsfield, A.J. & Bansemer, A. 2007 Snow size distribution parameterization for midlatitude and tropical ice clouds. *J. Atmos. Sci.* **64** (12), 4346–4365.

Garrett, T.J. & Yuter, S.E. 2014 Observed influence of riming, temperature, and turbulence on the fallspeed of solid precipitation. *Geophys. Res. Lett.* **41** (18), 6515–6522.

Gerashchenko, S., Sharp, N.S., Neuscamman, S. & Warhaft, Z. 2008 Lagrangian measurements of inertial particle accelerations in a turbulent boundary layer. *J. Fluid Mech.* **617**, 255–281.

Good, G.H., Ireland, P.J., Bewley, G.P., Bodenschatz, E., Collins, L.R. & Warhaft, Z. 2014 Settling regimes of inertial particles in isotropic turbulence. *J. Fluid Mech.* **759**, R3.

Heisel, M., Dasari, T., Liu, Y., Hong, J., Coletti, F. & Guala, M. 2018 The spatial structure of the logarithmic region in very-high-Reynolds-number rough wall turbulent boundary layers. *J. Fluid Mech.* **857**, 704–747.

Heymsfield, A.J. 1972 Ice crystal terminal velocities. *J. Atmos. Sci.* **29** (7), 1348–1357.

Heymsfield, A.J. & Westbrook, C.D. 2010 Advances in the estimation of ice particle fall speeds using laboratory and field measurements. *J. Atmos. Sci.* **67** (8), 2469–2482.

Hong, J., Toloui, M., Chamorro, L.P., Guala, M., Howard, K., Riley, S., Tucker, J. & Sotiropoulos, F. 2014 Natural snowfall reveals large-scale flow structures in the wake of a 2.5-MW wind turbine. *Nat. Commun.* **5** (1), 4216.

Jayaweera, K.O.L.F. & Mason, B.J. 1965 The behaviour of freely falling cylinders and cones in a viscous fluid. *J. Fluid Mech.* **22** (4), 709–720.

Kajikawa, M. 1976 Observation of falling motion of columnar snow crystals. *J. Meteorol. Soc. Japan* II **54** (5), 276–284.

Kajikawa, M. 1982 Observation of the falling motion of early snow flakes: Part. I. Relationship between the free-fall pattern and the number and shape of component snow crystals. *J. Meteorol. Soc. Japan* II **60** (2), 797–803.

Kajikawa, M. 1989 Observation of the falling motion of early snowflakes. Part II. On the variation of falling velocity. *J. Meteorol. Soc. Japan* II **67** (5), 731–738.

Kajikawa, M. 1992 Observations of the falling motion of plate-like snow crystals. Part I. The free-fall patterns and velocity. *J. Meteorol. Soc. Japan* II **70** (1), 1–9.

Kajikawa, M. & Okuhara, K. 1997 Observations of the falling motion of plate-like snow crystals. Part II. The free-fall patterns and velocity variations of rimed crystals. *J. Meteorol. Soc. Japan* II **75** (4), 811–818.

KASKAS, A.A. 1970 Schwarmgeschwindigkeiten in mehrkornsuspensionen am beispeil der sedimentation. PhD thesis, Berlin.

KHVOROSTYANOV, V.I. & CURRY, J.A 2005 Fall velocities of hydrometeors in the atmosphere: refinements to a continuous analytical power law. *J. Atmos. Sci.* **62** (12), 4343–4357.

KHVOROSTYANOV, V.I. & CURRY, J.A. 2002 Terminal velocities of droplets and crystals: power laws with continuous parameters over the size spectrum. *J. Atmos. Sci.* **59** (11), 1872–1884.

KLETT, J.D. 1995 Orientation model for particles in turbulence. *J. Atmos. Sci.* **52** (12), 2276–2285.

LEINONEN, J., GRAZIOLI, J. & ALEXIS, B. 2021 Reconstruction of the mass and geometry of snowfall particles from multi angle snowflake camera (MASC) images. *Atmos. Meas. Tech. Discuss.* **14** (10), 1–29.

LI, C., LIM, K., BERK, T., ABRAHAM, A., HEISEL, M., GUALA, M., COLETTI, F. & HONG, J. 2021*a* Settling and clustering of snow particles in atmospheric turbulence. *J. Fluid Mech.* **912**, A49.

LI, J., ABRAHAM, A., GUALA, M. & HONG, J. 2021*b* Evidence of preferential sweeping during snow settling in atmospheric turbulence. *J. Fluid Mech.* **928**, A8.

LI, J., GUALA, M. & HONG, J. 2023 Snow particle analyzer for simultaneous measurements of snow density and morphology. *J. Geophys. Res.* **128** (16), e2023JD038987.

LIBBRECHT, K.G. 2005 The physics of snow crystals. *Rep. Prog. Phys.* **68** (4), 855–895.

LOCATELLI, J.D. & HOBBS, P.V. 1974 Fall speeds and masses of solid precipitation particles. *J. Geophys. Res.* **79** (15), 2185–2197.

MAGONO, C. & LEE, C.W. 1966 Meteorological classification of natural snow crystals. *J. Fac. Sci. Hokkaido Univ. 7* **2** (4), 321–335.

MARCUS, G.G., PARSA, S., KRAMEL, S., NI, R. & VOTH, G.A. 2014 Measurements of the solid-body rotation of anisotropic particles in 3D turbulence. *New J. Phys.* **16** (10), 102001.

MARKS, D., KIMBALL, J., TINGEY, D. & LINK, T. 1998 The sensitivity of snowmelt processes to climate conditions and forest cover during rain-on-snow: a case study of the 1996 Pacific Northwest flood. *Hydrol. Process.* **12** (10–11), 1569–1587.

MAXEY, M.R. 1987 The gravitational settling of aerosol particles in homogeneous turbulence and random flow fields. *J. Fluid Mech.* **174**, 441–465.

MCCORQUODALE, M.W. & WESTBROOK, C.D. 2021 TRAIL part 2: a comprehensive assessment of ice particle fall speed parametrisations. *Q. J. R. Meteorol. Soc.* **147** (734), 605–626.

MEZIĆ, I., LEONARD, A. & WIGGINS, S. 1998 Regular and chaotic particle motion near a helical vortex filament. *Physica* D **111** (1–4), 179–201.

MITCHELL, D.L. & HEYMSFIELD, A.J. 2005 Refinements in the treatment of ice particle terminal velocities, highlighting aggregates. *J. Atmos. Sci.* **62** (5), 1637–1644.

NAKAYA, U. & TERADA, T. 1935 Simultaneous observations of the mass, falling velocity and form of individual snow crystals. *J. Fac. Sci. Hokkaido Univ.* **1** (7), 191–200.

NEMES, A., DASARI, T., HONG, J., GUALA, M. & COLETTI, F. 2017 Snowflakes in the atmospheric surface layer: observation of particle–turbulence dynamics. *J. Fluid Mech.* **814**, 592–613.

OGURA, T., KAGEYAMA, I., NASUKAWA, K., MIYASHITA, Y., KITAGAWA, H. & IMADA, Y. 2002 Study on a road surface sensing system for snow and ice road. *JSAE Rev.* **23** (3), 333–339.

PETERSEN, A.J., BAKER, L. & COLETTI, F. 2019 Experimental study of inertial particles clustering and settling in homogeneous turbulence. *J. Fluid Mech.* **864**, 925–970.

ROOS, F.W. & WILLMARTH, W.W. 1971 Some experimental results on sphere and disk drag. *AIAA J.* **9** (2), 285–291.

SCAGLIARINI, A. 2011 Geometric properties of particle trajectories in turbulent flows. *J. Turbul.* **12**, N25.

SCHANZ, D., GESEMANN, S. & SCHRÖDER, A. 2016 Shake-the-box: Lagrangian particle tracking at high particle image densities. *Exp. Fluids* **57**, 1–27.

SIEWERT, C., KUNNEN, R.P.J., MEINKE, M. & SCHRÖDER, W. 2014 Orientation statistics and settling velocity of ellipsoids in decaying turbulence. *Atmos. Res.* **142**, 45–56.

SINGH, D.K., PARDYJAK, E.R. & GARRETT, T.J. 2023 A universal scaling law for Lagrangian snowflake accelerations in atmospheric turbulence. *Phys. Fluids* **35** (12), 123336.

STEINKOGLER, W., SOVILLA, B. & LEHNING, M. 2014 Influence of snow cover properties on avalanche dynamics. *Cold Reg. Sci. Technol.* **97**, 121–131.

TAGLIAVINI, G., MCCORQUODALE, M., WESTBROOK, C., CORSO, P., KROL, Q. & HOLZNER, M. 2021*a* Drag coefficient prediction of complex-shaped snow particles falling in air beyond the Stokes regime. *Intl J. Multiphase Flow* **140**, 103652.

TAGLIAVINI, G., MCCORQUODALE, M., WESTBROOK, C. & HOLZNER, M. 2021*b* Numerical analysis of the wake of complex-shaped snow particles at moderate Reynolds number. *Phys. Fluids* **33** (10), 105103.

TAN, S., SALIBINDLA, A., MASUK, A.U.M. & NI, R. 2020 Introducing OpenLPT: new method of removing ghost particles and high-concentration particle shadow tracking. *Exp. Fluids* **61**, 1–16.

THERIAULT, D.H., FULLER, N.W., JACKSON, B.E., BLUHM, E., EVANGELISTA, D., WU, Z., BETKE, M. & HEDRICK, T.L. 2014 A protocol and calibration method for accurate multi-camera field videography. *J. Expl Biol.* **217** (11), 1843–1848.

TINKLENBERG, A., GUALA, M. & COLETTI, F. 2023 Thin disks falling in air. *J. Fluid Mech.* **962**, A3.

TOLOUI, M., RILEY, S., HONG, J., HOWARD, K., CHAMORRO, L.P., GUALA, M. & TUCKER, J. 2014 Measurement of atmospheric boundary layer based on super-large-scale particle image velocimetry using natural snowfall. *Exp. Fluids* **55** (5), 1737.

TOUPOINT, C., ERN, P. & ROIG, V. 2019 Kinematics and wake of freely falling cylinders at moderate Reynolds numbers. *J. Fluid Mech.* **866**, 82–111.

VOTH, G.A., LA PORTA, A., CRAWFORD, A.M., ALEXANDER, J. & BODENSCHATZ, E. 2002 Measurement of particle accelerations in fully developed turbulence. *J. Fluid Mech.* **469**, 121–160.

VOTH, G.A. & SOLDATI, A. 2017 Anisotropic particles in turbulence. *Annu. Rev. Fluid Mech.* **49**, 249–276.

WANG, L.-P. & MAXEY, M.R. 1993 Settling velocity and concentration distribution of heavy particles in homogeneous isotropic turbulence. *J. Fluid Mech.* **256**, 27–68.

WILLMARTH, W.W., HAWK, N.E. & HARVEY, R.L. 1964 Steady and unsteady motions and wakes of freely falling disks. *Phys. Fluids* **7** (2), 197–208.

WINKLER, R.L. 2015 The importance of communicating uncertainties in forecasts: overestimating the risks from winter storm Juno. *Risk Anal.* **35** (3), 349–353.

WU, Y., WU, X., YAO, L., BRUNEL, M., COËTMELLEC, S., LEBRUN, D., GRÉHAN, G. & CEN, K. 2015 Simultaneous measurement of 3D velocity and 2D rotation of irregular particle with digital holographic particle tracking velocimetry. *Powder Technol.* **284**, 371–378.

XU, H., OUELLETTE, N.T. & BODENSCHATZ, E. 2007 Curvature of Lagrangian trajectories in turbulence. *Phys. Rev. Lett.* **98** (5), 050201.

YANG, C.Y. & LEI, U. 1998 The role of the turbulent scales in the settling velocity of heavy particles in homogeneous isotropic turbulence. *J. Fluid Mech.* **371**, 179–205.